Colliding neutron stars

Gravitational waves, neutrino emission, and gamma-ray bursts

M. Ruffert[1⋆] and H.-Th. Janka[2⋆⋆]

[1] Institute of Astronomy, Madingley Road, Cambridge CB3 0HA, United Kingdom
[2] Max-Planck-Institut für Astrophysik, Postfach 1523, 85740 Garching, Germany

the date of receipt and acceptance should be inserted later

Abstract. Three-dimensional hydrodynamical simulations are presented for the direct head-on or off-center collision of two neutron stars, employing a basically Newtonian PPM code but including the emission of gravitational waves and their back-reaction on the hydrodynamical flow. A physical nuclear equation of state is used that allows us to follow the thermodynamical evolution of the stellar matter and to compute the emission of neutrinos. Predicted gravitational wave signals, luminosities and waveforms, are presented. The models are evaluated for their implications for gamma-ray burst scenarios. We find an extremely luminous outburst of neutrinos with a peak luminosity of more than $4 \cdot 10^{54}$ erg/s for several milliseconds. This leads to an efficiency of about 1% for the annihilation of neutrinos with antineutrinos, corresponding to an average energy deposition rate of more than 10^{52} erg/s and a total energy of about 10^{50} erg deposited in electron-positron pairs around the collision site within 10 ms. Although these numbers seem very favorable for gamma-ray burst scenarios, the pollution of the $e^{\pm}$ pair-plasma cloud with nearly $10^{-1}\,M_{\odot}$ of dynamically ejected baryons is 5 orders of magnitude too large. Therefore the formation of a relativistically expanding fireball that leads to a gamma-ray burst powered by neutrino emission from colliding neutron stars is definitely ruled out.

Key words: gamma rays: bursts – gravitation: waves – elementary particles: neutrinos – stars: neutron – binaries: close – hydrodynamics

1. Introduction

The *merging* of two neutron stars that make up a binary system is of interest both because it is a powerful source of gravitational waves and because it might be the central engine of gamma-ray bursts. These mergings have been studied intensely during the past few years, since the occurrence rate is high enough (e.g. Narayan et al. 1991, Phinney 1991, Tutukov et al. 1992, Tutukov & Yungelson 1993, Lipunov et al. 1995, van den Heuvel & Lorimer 1996, Lipunov et al. 1997, Prokhorov et al. 1997, Bethe & Brown 1998) that one might be able to measure the observable consequences. However, direct *collisions* of two neutron stars are much rarer [the rate is $\ll 10^{-10}$ per year per galaxy (Centrella & McMillan 1993) as compared to the binary merger rate of 10^{-6} to 10^{-5} per year per galaxy] and thus have not received much attention.

Two previously published sets of hydrodynamical models of colliding neutron stars were computed by Centrella & McMillan (1993) and by Rasio & Shapiro (1992). Both used an SPH code to simulate the dynamics of two polytropic neutron stars of equal masses with adiabatic index $\gamma = 2$ and started at an initial distance of about four neutron star radii on parabolic orbits. Using a relatively small number of particles (2048), Centrella & McMillan (1993) were able to produce a catalog of gravitational wave luminosities and gravitational waveforms for different impact parameters. Rasio & Shapiro (1992) restricted themselves to fewer simulations with higher resolution (16000 particles) of neutron star coalescence as well as head-on collisions. They found that up to 5% of the total mass can escape from the systems and that strong shocks occur. Their results for the gravitational waveforms and luminosities reveal a smaller first maximum (caused by the initial free fall of the two stars), followed by the main peak associated with the rapid deceleration of the colliding matter during the propagation of the recoil shocks.

Neutron star collisions have repeatedly been suggested in the literature as possible sources of gamma-ray bursts (e.g., Katz & Canel 1996, Dokuchaev& Eroshenko 1996; also Dokuchaev et al. 1998), powered either by neutrino-antineutrino annihilation which produces an $e^{\pm}$ pair-photon fireball, or by highly relativistic shocks which are formed during the collision (or coalescence) and eject matter at relativistic velocities (Shaviv & Dar 1995). Katz & Canel

Send offprint requests to: H.-Th. Janka
⋆ e-mail: `mruffert@ast.cam.ac.uk`
⋆⋆ e-mail: `thj@mpa-garching.mpg.de`

(1996), in particular, developed the idea that long gamma-ray bursts might be explained by accretion induced collapse of bare degenerate white dwarfs, while short bursts might originate from neutron star *collisions*. They estimated the post-collision temperature to be $kT \approx 100\,\mathrm{MeV}$, and expected a neutrino pulse with a width of 2.5 ms, and a total number of escaping neutrinos of 10^{58} (refering to Dar et al. 1992). With a mean neutrino energy of about 6 MeV this corresponds to a total energy of 10^{53} erg emitted in neutrinos. They sketched the picture that shortly after the collision, dense lumps of hot matter expand and become optically thin to neutrinos which are released in a powerful outburst that is luminous enough to produce the desired gamma-ray burst energy by neutrino-antineutrino annihilation if one assumes an efficiency of 1%. In order to obtain the observed gamma-ray burst rates they had to invoke a total of 10^9 hypothetical clusters within $z \approx 1$ with 10^8 neutron stars each. They stated that "we cannot exclude the possibility that such clusters are commonly found at the centers of galaxies".

Neutron star collisions might also be considered as interesting, because they could be viewed at as more violent variants of the merging process with a more extreme dynamical evolution. This might support the formation of relativistic shocks and possibly lead to a larger burst of gravitational waves and neutrinos. More violence of the merging process can be expected from general relativistic effects which were so far neglected in the large majority of simulations (see, however, Wilson et al. 1996 for an interesting step towards fully general relativistic modeling). Oohara & Nakamura (1997), using a grid-based TVD scheme, performed preliminary simulations to compare the coalescence with a Newtonian potential to the case with post-Newtonian physics. Their neutron stars were modeled as two polytropes with $\gamma = 2$, $M = 0.62\,M_\odot$, and $R = 15\,\mathrm{km}$. The principal difference between the two cases was that the post-Newtonian merging indeed turned out to be more violent: the impact is more central and shocks develop, because "general relativity effectively increases the gravitational force". Although the strong shock itself has little immediate effect on the gravitational waveform, the dynamics can be changed because of the higher temperatures and densities. Wex (1995) and Ogawaguchi & Kojima (1996) showed that both spin-orbit and spin-spin interactions appear formally to be *first* order post-Newtonian corrections, just as gravitational potential corrections are (gravitational waves are 2.5 PN), but the inferred magnitude of these corrections for known compact binary systems is actually smaller.

Our project of simulating neutron star collisions with a Newtonian PPM code was motivated by the aspects described in the last two paragraphs. On the one hand, we intended to put potential gamma-ray burst scenarios to a test, on the other hand we wanted to study a situation that mimics the *merging* of two neutron stars with extreme violence and maximal parameters like pre-merging kinetic energy and angular momentum in the system. Thus we hoped not only to obtain an upper bound on the gravitational wave emission to be expected from the merging of two neutron stars, even with general relativistic effects included. We also wanted to see whether the most extreme conditions during the collision of the two stars lead to sufficiently large neutrino emission to explain the gamma-ray burst energetics by the annihilation of neutrinos and antineutrinos emitted during the dynamical event. The latter seems impossible in case of the final stages of the coalescence of binary neutron stars because the prompt neutrino burst, although very luminous, fails by several orders of magnitude to produce about 10^{51} erg of gamma-rays within the short time of only a few milliseconds that it takes the two neutron stars to merge into one massive body that is most likely going to collapse into a black hole on a dynamical timescale (Ruffert et al. 1996).

The paper is organized as follows. In Sect. 2 the basic aspects and new elements of our computational method (in extension of Ruffert et al. 1996) and the chosen initial conditions for our simulations are given. Our results are presented in the following sections, where we describe the hydrodynamical and thermodynamical evolution (Sect. 3), the gravitational wave emission (Sect. 4), and the neutrino production (Sect. 5) in the colliding stars together with the evaluation of our models for the efficiency of neutrino-antineutrino annihilation (Sect. 6). Section 7 contains a summary and conclusions.

2. Computational procedure and initial conditions

In this section we summarize the numerical methods and the treatment of the input physics used for the presented simulations. In addition, we specify the initial conditions by which our different models are distinguished. More detailed information about the employed numerical procedures can be found in RJS (Ruffert et al. 1996) and RJTS (Ruffert et al. 1997).

2.1. Hydrodynamical code

The hydrodynamical simulations were done with a code based on the Piecewise Parabolic Method (PPM) developed by Colella & Woodward (1984). The code is basically Newtonian, but contains the terms necessary to describe gravitational-wave emission and the corresponding back-reaction on the hydrodynamical flow (Blanchet et al. 1990). The modifications that follow from the gravitational potential are implemented as source terms in the PPM algorithm. The necessary spatial derivatives are evaluated as standard centered differences on the grid.

In order to describe the thermodynamics of the neutron star matter, we use the equation of state (EOS) of Lattimer & Swesty (1991) for a compressibility modulus

Table 1. Characterizing parameters and some computed quantities for all models. N is the number of grid zones per dimension, L the size of the largest grid, l the size of the smallest zone, $M_{\rho<11}$ the gas mass with density below 10^{11} g/cm^3 at the end of the simulation, and $M_{\rm d}$ the mass with specific angular momentum larger than $j^* \equiv v_{\rm Kepler}(3R_{\rm s})3R_{\rm s}$ where $R_{\rm s}$ is the event horizon of a $\sim 3\,M_\odot$ black hole probably forming from the colliding neutron stars. $M_{\rm g}$ denotes the mass swept off the grid, $M_{\rm u}$ is the mass leaving the grid unbound, and $T_{\rm ex}$ the maximum temperature (in energy units) reached on the grid during the simulation of a model.

Model	impact direction	spin	N	L km	l km	$M_{\rho<11}$ $10^{-2}M_\odot$	$M_{\rm d}$ $10^{-2}M_\odot$	$M_{\rm g}$ $10^{-2}M_\odot$	$M_{\rm u}$ $10^{-2}M_\odot$	$T_{\rm ex}$ MeV
h	head-on	none	32	328	1.28	4.0	0.0	5.2	1.5	96.
H	head-on	none	64	328	0.64	4.1	0.0	6.6	1.5	96.
$\mathcal{H}$	head-on	none	128	328	0.32	—	—	—	—	—
o	off-center	none	32	328	1.28	9.0	0.03	1.5	0.16	57.
O	off-center	none	64	328	0.64	11.0	0.03	1.8	0.19	58.

Table 2. Gravitational-wave and neutrino emission properties for all models. $\widehat{\mathcal{L}}$ is the maximum gravitational-wave luminosity, $\mathcal{E}$ the total energy emitted in gravitational waves, $\widehat{rh}$ the maximum amplitude of the gravitational waves as observed from a distance r, L_{ν_e} the stationary value of the electron neutrino luminosity which is reached at about 6–10 ms after the start of the simulations, $L_{\bar\nu_e}$ the corresponding electron antineutrino luminosity, and L_{ν_x} the luminosity of each individual species of ν_x $(=\nu_\mu, \bar\nu_\mu, \nu_\tau, \bar\nu_\tau)$. L_ν represents the total neutrino luminosity at the end of the simulation, $\langle\epsilon_{\nu_e}\rangle$, $\langle\epsilon_{\bar\nu_e}\rangle$ and $\langle\epsilon_{\nu_x}\rangle$ are the mean energies of the different neutrino and antineutrino flavors. $\dot E_{\nu\bar\nu}$ denotes the integral rate of energy deposition by neutrino-antineutrino annihilation, averaged over the simulation time of 10 ms.

Model	impact direction	$\widehat{\mathcal{L}}$ $10^{55}\,\frac{\rm erg}{\rm s}$	$\mathcal{E}$ 10^{52} erg	$\widehat{rh}$ 10^4cm	L_{ν_e} $10^{53}\,\frac{\rm erg}{\rm s}$	$L_{\bar\nu_e}$ $10^{53}\,\frac{\rm erg}{\rm s}$	L_{ν_x} $10^{53}\,\frac{\rm erg}{\rm s}$	L_ν $10^{53}\,\frac{\rm erg}{\rm s}$	$\langle\epsilon_{\nu_e}\rangle$ MeV	$\langle\epsilon_{\bar\nu_e}\rangle$ MeV	$\langle\epsilon_{\nu_x}\rangle$ MeV	$\dot E_{\nu\bar\nu}$ $10^{50}\,\frac{\rm erg}{\rm s}$
h	head-on	4.2	0.42	6.3	2.4	5.0	1.4	13.	14.	20.	26.	—
H	head-on	3.61	0.39	6.2	2.0	4.0	1.0	10.	13.	20.	25.	100
$\mathcal{H}$	head-on	3.55	—	6.2	—	—	—	—	—	—	—	—
o	off-center	6.6	4.1	12.3	1.3	2.8	0.8	7.3	11.	18.	25.	—
O	off-center	6.1	3.6	11.9	1.2	3.1	0.8	7.5	11.	18.	25.	—

of bulk nuclear matter of $K = 180\,$MeV in tabular form. Energy loss and changes of the electron abundance due to the emission of neutrinos and antineutrinos are taken into account by an elaborate "neutrino leakage scheme". The energy source terms contain the production of all types of neutrino pairs by thermal processes and additionally of electron neutrinos and antineutrinos by lepton captures onto baryons. The latter reactions act as sources or sinks of lepton number, too, and are included as source terms in a continuity equation for the electron lepton number. Matter is rendered optically thick to neutrinos due to the main opacity producing reactions which are neutrino-nucleon scattering and absorption of electron-type neutrinos onto nucleons.

More detailed information about the employed numerical procedures can be found in RJS, in particular about the implementation of the gravitational-wave radiation and back-reaction terms and the treatment of the neutrino lepton number and energy loss terms in the hydrodynamical code.

We have extended and improved the numerical treatment as compared to RJS in several aspects (a comparison of published results for coalescing neutron stars obtained with the old code against results from the improved one will be given in a separate, forthcoming paper):

(a) Numerical resolution: The presented simulations were done on multiply nested and refined grids. With an only modest increase in CPU time, the nested grids allow one to simulate a substantially larger computational volume while at the same time they permit a higher local spatial resolution of the merged object. The former is important to follow the fate of matter that is flung out to distances far away from the collision site either to become unbound or to eventually fall back. The latter is necessary to adequately resolve the strong shock fronts and steep discontinuities of the plasma flow that develop during the collision. The procedures used here are based on the algorithms that can be found in Berger & Colella (1989), Berger (1987) and Berger & Oliger (1984). Our version is described in detail in Section 4 of Ruffert (1992) so only the most important features are to be summarized here. The individual grids are equidistant and Cartesian with each finer grid having a factor of two smaller zone size and extent than the next coarser one. Hereby the number of zones remains the same for all grids, typically 32^3 for low-resolution test calculations, 64^3 for our "standard"

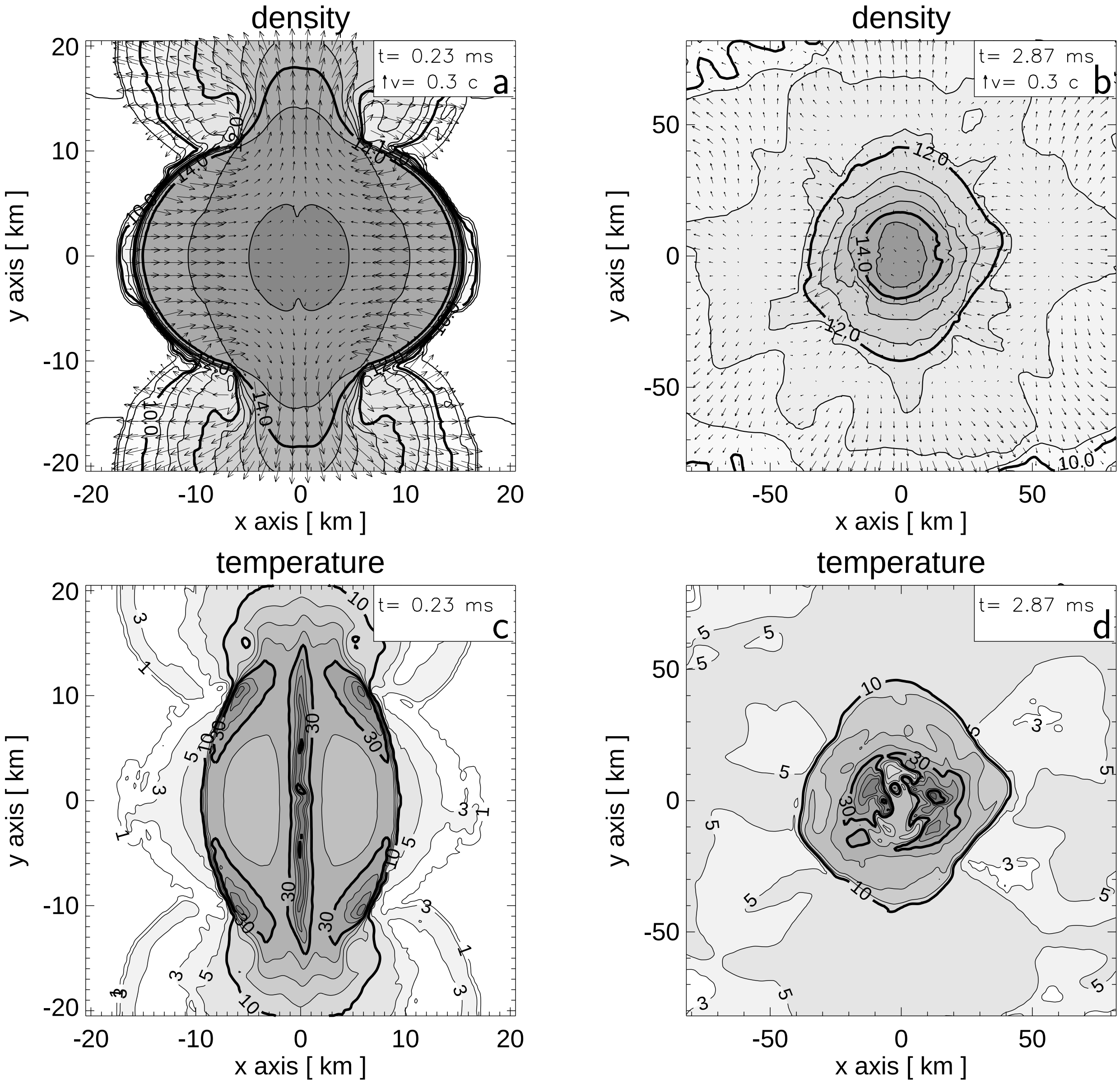

Fig. 1. Contour plots of Model $\mathcal{H}$ (left panels) and H (right panels) showing cuts in a plane containing the x-axis which is the symmetry axis of the initial model. The displayed physical quantities are the density together with the velocity field (panels a and b) and the temperature (panels c and d). The density is measured in $\mathrm{g\,cm^{-3}}$, the temperature in MeV. The density contours are spaced logarithmically with intervals of 0.5 dex, while the temperature contours are linearly spaced, starting with 1 MeV, 3 MeV, 5 MeV, and then continuing with an increment of 5 MeV. The bold contours are labeled with their corresponding values (10^{10}, 10^{12}, and $10^{14}\,\mathrm{g\,cm^{-3}}$, and 10, 30, and 50 MeV, respectively). In the box in the upper right corner of each panel, the velocity vectors and the time elapsed since the beginning of the simulation are given. The mirror symmetry relative to the plane $x = 0$ and the rotational symmetry around the x-axis are broken during the evolution (panels b and d) because of an instability of the contact layer of the two neutron stars against shear motions by which numerical fluctuations (panel c) are amplified.

simulations, and 128^3 for models of special interest where high resolution seems desirable.

(b) Physics input: The table for the Lattimer & Swesty (1991) equation of state was extended to higher and lower temperatures and now spans $0.01\,\mathrm{MeV} \leq T \leq 100\,\mathrm{MeV}$, and also the lower density bound was moved down to now $\rho_{\min} = 5\cdot 10^7\,\mathrm{g\,cm^{-3}}$ so that the density range now covered by the table is $5\cdot 10^7\,\mathrm{g\,cm^{-3}} \leq \rho \leq 2.9\cdot 10^{15}\,\mathrm{g\,cm^{-3}}$.

2.2. Evaluation of neutrino-antineutrino annihilation

In a post-processing step, performed after the hydrodynamical evolution had been calculated, we evaluated our models for neutrino-antineutrino ($\nu\bar{\nu}$) annihilation in the surroundings of the collided stars in order to construct a map showing the local energy deposition rates per unit volume. Spatial integration finally yields the total rate of energy deposition outside the neutrino emitting high-

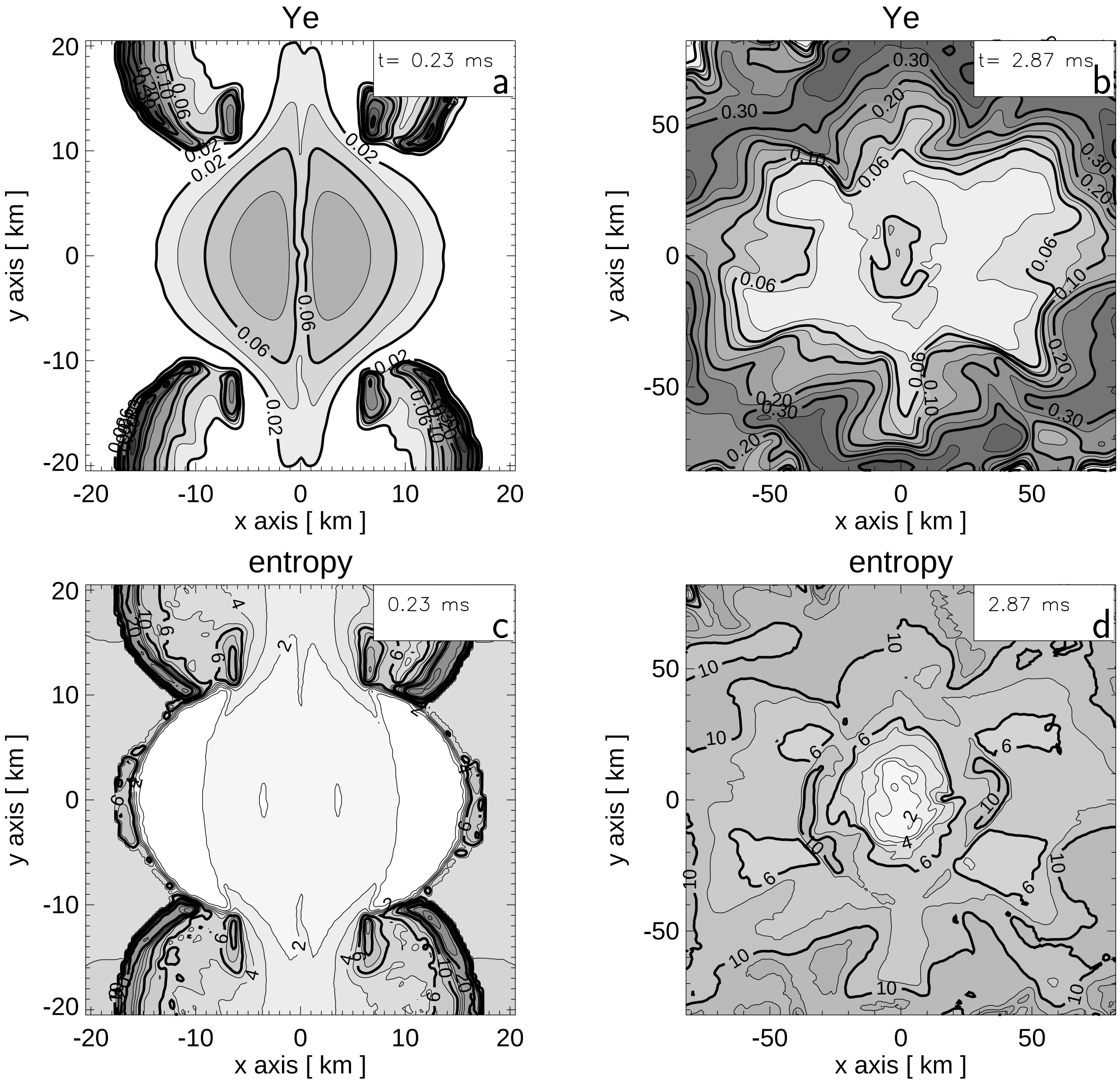

Fig. 2. Contour plots of Model $\mathcal{H}$ (left panels) and H (right panels) showing cuts in a plane containing the x-axis which is the symmetry axis of the initial model. The displayed physical quantities are the electron fraction Y_e (panels a and b) and the entropy (panels c and d), the latter measured in units of Boltzmann's constant k per nucleon. The contours of the electron fraction are linearly spaced with intervals of 0.02 below 0.1 and with intervals of 0.05 above, the entropy contours are given in steps of $1\,k$/nucleon from 1 to 6, in steps of $2\,k$/nucleon between 6 and 16, and then for values of 20, 25, 30, and $40\,k$/nucleon. The bold contours are labeled with their corresponding values (0.02, 0.06, 0.10, 0.20, 0.30, and 0.40 for Y_e, and 6, 10, and 20 for the entropy). Maximum values of Y_e are above 0.4, of the entropy near $30\,k$/nucleon. In the box in the upper right corner of each panel, the time elapsed since the beginning of the simulation is given.

density regions. The "brute force" approach, however, which was applied by RJTS, is not feasible any longer because it involved explicit summation of the contributions of neutrino and antineutrino loss terms of all grid cells and at every location where the local annihilation rate was to be determined. The computational load for this procedure increases roughly with the third power of the number of grid zones if the annihilation map has about the same spatial resolution as the grid for the hydrodynamical simulation. With the larger number of zones on several levels of the nested grid, such a strategy is currently computationally impossible.

Therefore we resort to a different approach which involves five distinct steps. (1) First, the relevant physical quantities are mapped from only that fractional volume of the nested grids where most of the neutrino emission (and neutrino opacity) comes from, to an equidistant Cartesian grid of fairly high resolution (typically 140^3). This

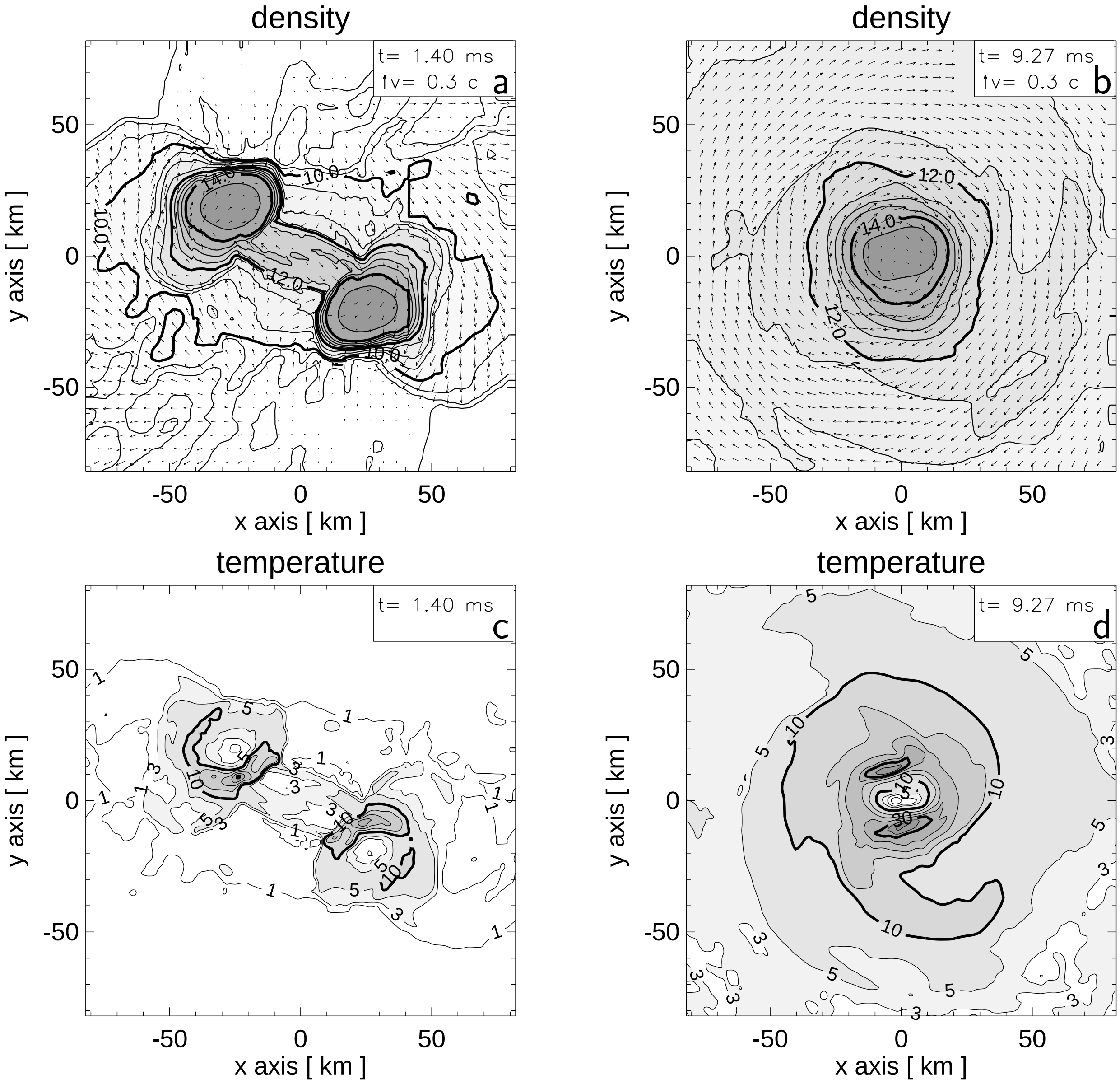

Fig. 3. Contour plots of Model O showing cuts in the orbital plane for the density together with the velocity field (panels a and b) and for the temperature (panels c and d). The density is measured in $\mathrm{g\,cm^{-3}}$, the temperature in MeV. The density contours are spaced logarithmically with intervals of 0.5 dex, while the temperature contours are linearly spaced, starting with 1 MeV, 3 MeV, 5 MeV, and then continuing with an increment of 5 MeV. The bold contours are labeled with their corresponding values (10^{10}, 10^{12}, and $10^{14}\,\mathrm{g\,cm^{-3}}$, and 10, 30, and 50 MeV, respectively). In the box in the upper right corner of each panel, the velocity vectors and the time elapsed since the beginning of the simulation are given.

mapping is done by tri-linear interpolation. (2) Second, on this grid, the neutrinosphere for each flavor of neutrino or antineutrino ν_i is determined. We define this two-dimensional hypersurface for ν_i by the set of those triples (x, y, z) where, for each chosen pair of coordinates x and y, the vertical optical depth $\tau_{\nu_i}(z)$ satisfies the condition $\tau_{\nu_i}(z) = \Delta z \cdot \sum_{j=z}^{\infty} \kappa_i(j) = 1$ where Δz is the cell size of the Cartesian grid and $\kappa_i(j)$ the local opacity of neutrino ν_i at position j. (3) Thirdly, the local neutrino number and energy loss terms of neutrino ν_i are added up along the z-direction (for each fixed pair (x, y)), and the total neutrino emissivity and the corresponding average energy of the emitted neutrinos are projected to originate from the neutrinosphere of neutrino ν_i determined in step (2). (4) Fourthly, and most importantly, the energy deposition rates by $\nu\bar{\nu}$ annihilation are calculated by integrating (summing) only over the two-dimensional neutrinospheres as neutrino and antineutrino sources instead of the three-dimensional stellar volume as done in RJTS. Additional conditions imposed on the construction of the annihilation map by RJTS are also used here, i.e., the neutrino emission is assumed to occur isotropically around the *outward*

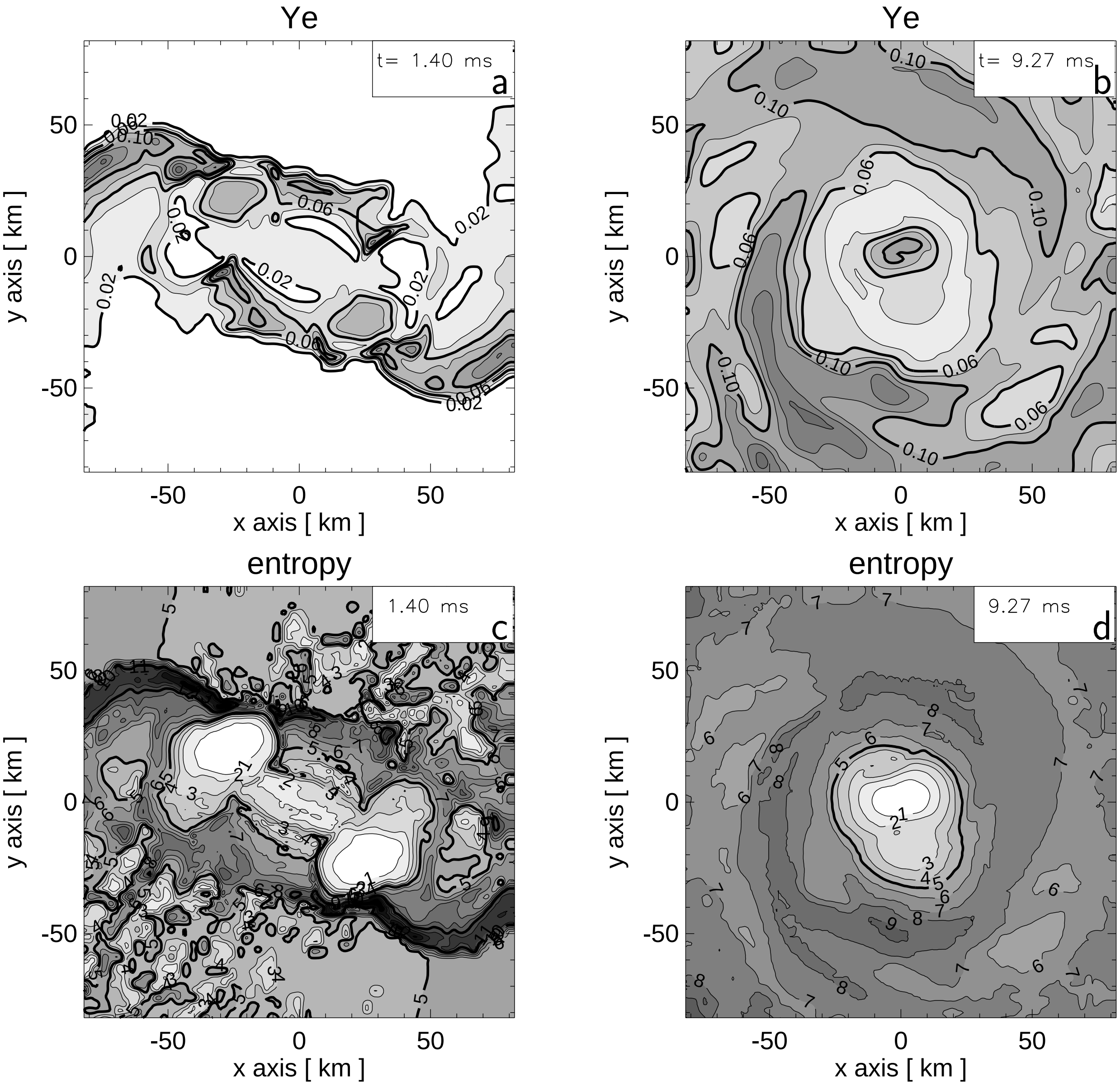

Fig. 4. Contour plots of Model O showing cuts in the orbital plane for the electron fraction Y_e (panels a and b) and the entropy (panels c and d), the latter quantity measured in units of Boltzmann's constant k per nucleon. The contours are linearly spaced with intervals of 0.02 for the electron fraction and $1\,k$/nucleon for the entropy. The bold contours are labeled with their corresponding values (0.02, 0.06, 0.10, 0.20 for Y_e and 5 and 10 for the entropy). Maximum values of Y_e are around 0.16, of the entropy about $10\,k$/nucleon. In the box in the upper right corner of each panel, the time elapsed since the beginning of the simulation is given.

pointing local density gradients at the neutrinospheres, and the energy deposition by $\nu\bar{\nu}$ annihilation is evaluated only in those regions where the baryon density is below a certain threshold, typically $\rho < 10^{11}\,\mathrm{g\,cm^{-3}}$, and on a cylindrical grid with coarser resolution than the Cartesian grid used to represent the neutrino sources, in order to limit the costs of the numerically intense calculations. (5) Finally, the local energy deposition rates per unit volume, $\dot{E}_{\rm ann}(\varpi,\phi,z)$, are averaged over the ϕ direction of the cylindrical grid:

$$\dot{E}_{\rm ann}(\varpi,z) = \frac{1}{2\pi}\int_0^{2\pi} \dot{E}_{\rm ann}(\varpi,\phi,z)\,\mathrm{d}\phi\,. \qquad (1)$$

From these average values two-dimensional maps like the one shown in Sect. 6 are plotted and integral numbers can be obtained by summation along radial or vertical directions in the cylindrical grid.

The total energy deposition rate ("annihilation luminosity") $L_{\rm ann}$ is obtained from the local values of the energy deposition rate per unit volume, $\dot{E}_{\rm ann}(\varpi,z)$, by inte-

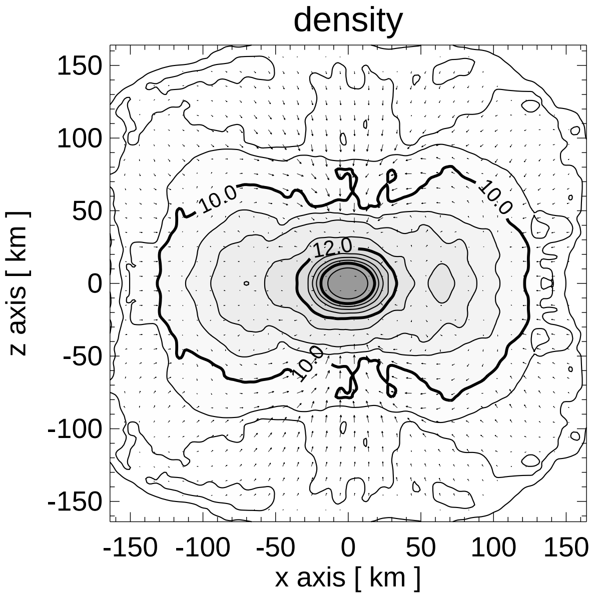

Fig. 5. Cut through Model O showing the density contours together with the velocity field in the plane $y = 0$ perpendicular to the orbital plane near the end of the simulation ($t = 9.27$ ms). The contours are spaced logarithmically with intervals of 0.5 dex, the bold contours correspond to density values of 10^{10}, 10^{12}, and 10^{14} g cm^{-3}, respectively. The velocity vectors are normalized as in Fig. 3b.

gration over the whole space outside the neutrino emitting stellar source:

$$L_{\rm ann} = \int \dot{E}_{\rm ann}(\varpi, \phi, z)\,{\rm d}V \tag{2}$$

with ${\rm d}V = \varpi\,{\rm d}\varpi\,{\rm d}\phi\,{\rm d}z$. Given the time dependent function $L_{\rm ann}(t)$ one can then calculate the cumulative energy deposition by neutrino-antineutrino annihilation according to

$$E_{\rm ann} = \int L_{\rm ann}(t)\,{\rm d}t\,. \tag{3}$$

Because the computation is so expensive, however, $L_{\rm ann}(t)$ cannot be evaluated on a fine temporal grid, but only at a few discrete points in time, t_i. With the values $L_{\rm ann}(t_i)$ we therefore make the following approximation for $E_{\rm ann}$:

$$E_{\rm ann} \approx \frac{1}{N}\sum_{i=1}^{N}\left(\frac{L_{\rm ann}(t_i)}{\mathcal{F}(t_i)}\right)\cdot\int \mathcal{F}(t)\,{\rm d}t \tag{4}$$

where $\mathcal{F}(t)$ is defined by

$$\begin{aligned}\mathcal{F}(t) \equiv\ & \frac{1}{R(t)}\Big\{L_{\nu_e}(t)\,L_{\bar\nu_e}(t)\,\left[\langle\epsilon_{\nu_e}(t)\rangle + \langle\epsilon_{\bar\nu_e}(t)\rangle\right] + \\ & 2\cdot L_{\nu_\mu}(t)\,L_{\bar\nu_\mu}(t)\,\left[\langle\epsilon_{\nu_\mu}(t)\rangle + \langle\epsilon_{\bar\nu_\mu}(t)\rangle\right]\Big\}\,. \end{aligned}\tag{5}$$

Here the term multiplied by the factor 2 accounts for the equal contributions from $\nu_\mu\bar\nu_\mu$ annihilation and $\nu_\tau\bar\nu_\tau$ annihilation. The form of $\mathcal{F}(t)$ in Eq. (5) reflects the main dependences of the $\nu\bar\nu$ annihilation rate: The energy deposition rate increases proportional to the product of the neutrino and antineutrino luminosities times the sum of the mean energies of the annihilating neutrinos and antineutrinos; in the denominator the characteristic radial extent $R(t)$ of the neutrino source comes from the volume integral of Eq. (2) when the latter is performed in spherical coordinates (compare Eqs. (3) and (10) in RJTS and references therein). The ratio appearing in Eq. (4) in the sum in front of the time integral then contains geometrical effects which result from the dependence of the $\nu\bar\nu$ annihilation rate on the angular distributions of neutrinos and antineutrinos. From the hydrodynamical models, the neutrino luminosities for the individual neutrino flavors, $L_{\nu_e}(t)$, $L_{\bar\nu_e}(t)$ and the corresponding values for muon and tau neutrinos and antineutrinos, are available as functions of time as well as the average energies of the emitted neutrinos, $\langle\epsilon_{\nu_e}(t)\rangle$, $\langle\epsilon_{\bar\nu_e}(t)\rangle$, and $\langle\epsilon_{\bar\nu_x}(t)\rangle$ for ν_μ, $\bar\nu_\mu$, ν_τ, and $\bar\nu_\tau$. We found that the typical radial size $R(t)$ of the neutrino emitting object during the phase where by far most of the $\nu\bar\nu$ annihilation happens is not very strongly time-dependent because the wobblings and oscillations change the shape and size of the collision remnant only on smaller scales but not globally. Therefore instead of $\mathcal{F}(t)$ from Eq. (5) we use in Eq. (4) the simpler expression

$$\begin{aligned}\mathcal{F}^*(t) \equiv\ & L_{\nu_e}(t)\,L_{\bar\nu_e}(t)\,\left[\langle\epsilon_{\nu_e}(t)\rangle + \langle\epsilon_{\bar\nu_e}(t)\rangle\right] + \\ & 2\cdot L_{\nu_\mu}(t)\,L_{\bar\nu_\mu}(t)\,\left[\langle\epsilon_{\nu_\mu}(t)\rangle + \langle\epsilon_{\bar\nu_\mu}(t)\rangle\right]\,. \end{aligned}\tag{6}$$

Computing $E_{\rm ann}$ from Eq. (4) instead of Eq. (3) involves the approximation that the term abbreviated by $\mathcal{F}(t)$ or $\mathcal{F}^*(t)$ contains the main time dependence of the integral in Eq. (3). Ideally, the ratio $L_{\rm ann}(t)/\mathcal{F}^*(t)$ would have to be constant. Since this is not the case, we decided to employ an average value for a small number N of time points where the spatial integral of Eq. (2) was evaluated. It turned out that the variation of $L_{\rm ann}(t)/\mathcal{F}^*(t)$ during the most interesting phase of the evolution is less than a factor 2.

2.3. Initial conditions

We started our simulations with two identical Newtonian neutron stars, each having a baryonic mass of about 1.63 $M_\odot$ and a radius of 15 km, which were placed at a center-to-center distance of 42 km. The distributions of density ρ and electron fraction $Y_e \equiv n_e/n_b$ (with n_e being the number density of electrons minus that of positrons, and n_b the baryon number density) were taken from a one-dimensional model of a cold, deleptonized neutron star in hydrostatic equilibrium and were the same as in RJS. For numerical reasons the surroundings of the neutron stars cannot be treated as completely evacuated. The density of the ambient medium was set to less than 10^8 g/cm^3, more than six orders of magnitude smaller than the central densities of the stars. The total mass on the whole grid, associated with this finite density is less than $10^{-3}\,M_\odot$.

The neutron stars were given the free-fall velocity at their respective initial positions $(x, y, z) = (-21\,{\rm km}, 0, 0)$

and $(x,y,z) = (21\,\mathrm{km}, 0, 0)$. The angle between the velocity vectors and the vector connecting the stellar centers was varied to produce a head-on collision for Models h, H, and $\mathcal{H}$, and an off-center collision for Models o and O. The impact parameter of the latter was chosen to be one neutron star radius. This impact parameter is the minimum distance that two point masses reach along their orbits. A compilation of all models together with their characterizing grid parameters, initial parameter settings, and some results of the numerical simulations is given in Tables 1 and 2.

In degenerate matter variations of the temperature lead only to minor changes of the internal energy and pressure (both are dominated by degeneracy effects) or, inversely, the temperature is extremely sensitive to small variations of the total internal energy. Therefore any small fluctuation caused for example by small numerical errors in the calculation of the energy density, will be amplified and reflected in temperature fluctuations. Subsequently, the neutrino emission, which scales with a high power of the temperature T, will be very noisy. For this reason we did not start our simulations with cold ($T = 0$) or "cool" ($T \lesssim 10^8$ K) neutron stars as suggested by the investigations of Kochanek (1992), Bildsten & Cutler (1992), and Lai (1994). Instead, we constructed initial temperature distributions inside the neutron stars by assuming thermal energy densities of about 3% of the degeneracy energy density for a given density ρ and electron fraction Y_e. The corresponding central temperature was around 7 MeV, the surface temperature less than half an MeV, and the average temperature was a few MeV. Because of the small contribution of thermal effects to the pressure, these temperatures are unimportant for the neutron star structure, and the rapid and violent hydrodynamical evolution ensures that the results are essentially unaffected by the assumed finite initial temperatures.

The simulations were performed on a Cray-YMP 4/64. The models with 64 zones needed about 24 MWords of main memory and took approximately 160 CPU-hours each, models with 32 zones roughly a factor of 10 less. Movies were generated for every model.

3. Hydrodynamical and thermodynamical evolution

3.1. Head-on collision

Figures 1 and 2 show the density ρ, temperature T, electron fraction Y_e, and entropy s at two different moments of the collision: At $t = 0.23\,\mathrm{ms}$ after the start of the simulation the largest compression is reached with a maximum density of $1.1 \cdot 10^{15}\,\mathrm{g\,cm^{-3}}$ (see Fig. 8), associated with a prominent peak of the gravitational wave luminosity (see Figs. 15 and 17), and at $t = 2.87\,\mathrm{ms}$ when the collision remnant has performed several cycles of oscillatory motions before it begins to settle into a more quiet state, and the neutrino emission starts to decrease from its most powerful phase (Figs. 20 and 22). For the earlier time, data from the high-resolution Model $\mathcal{H}$ are plotted in Figs. 1 and 2, whereas for the later moment only data from the 64^3 Model H are available.

Shortly after the surfaces of the neutron stars have touched during their head-on collision (Figs. 1a and 1c), a strong shock wave is generated at the common surface by the abrupt deceleration of the matter. This shock propagates back into the as yet practically undisturbed neutron star matter. The temperatures directly behind this shock reach values of more than 45 MeV, while ahead of the shock they were around 5 MeV. The entropy in the initially cool neutron star ($s \ll 1\,k/\mathrm{nucleon}$) is increased to values between $1\,k/\mathrm{nucleon}$ and $2\,k/\mathrm{nucleon}$ (Fig. 2c). At the same time, matter is being squeezed out perpendicularly to the collision axis and expands behind a very strong shock (postshock entropies near $30\,k/\mathrm{nucleon}$). This shock-heated matter emits electron antineutrinos in large numbers (cf. Fig. 22) and quickly develops from initially neutron-rich conditions to a much more symmetric nuclear state characterized by an electron fraction $Y_e \gtrsim 0.4$ (Fig. 2a). In contrast, in the interior of the colliding bodies the composition remains essentially unchanged because of the long neutrino diffusion timescales in the hot neutron star matter.

At the collision interface a thin "pancake" like layer with very high temperatures up to about 70 MeV (Figs. 1c and 9) occurs. This sheet is dynamically unstable due to shear motions. First indications of a break-down of the mirror symmetry relative to the y-z-plane can be already seen at $t = 0.23\,\mathrm{ms}$ in Figs. 1c and 2a. Only a short moment later, when the merged bodies bounce back and the oblate shape changes into a prolate form, this flat pancake-like layer folds asymmetrically and breaks up on a millisecond timescale (Fig. 1d). Within 3 ms the density distribution has already smoothed into a nearly spherical shape (Fig. 1b) and most of the kinetic energy of the impact has been dissipated by shocks into thermal energy or is carried away by ejected matter (see Fig. 12). The collision has lead to an increase of the entropy to values near $2\,k/\mathrm{nucleon}$ in the merged object (Fig. 2c), whereas the shock heated gas that forms a very extended, nearly spherical cloud around the dense central body, has entropies between $6\,k/\mathrm{nucleon}$ and $10\,k/\mathrm{nucleon}$ (Fig. 2d). Ejected clumps of matter with even higher entropy ($s \sim 20\,k/\mathrm{nucleon}$) can be identified, and positron captures onto neutrons and $\bar{\nu}_e$ production in the hot gas ($T \sim$ several MeV) leads to a rapid increase of the electron fraction to values $Y_e \sim 0.3$–0.4 and higher in the expanding debris.

The formation of shock waves at the moment of the impact in Model H (Fig. 1) clearly indicates that the head-on collision is strongly inelastic and the dissipation of kinetic energy happens very efficiently. Therefore the two neutron stars are not able to separate again after the first compression and reexpansion, however, it takes several (4–6)

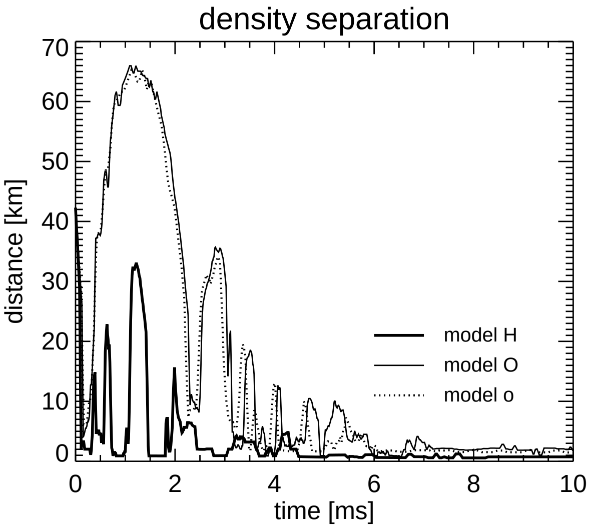

Fig. 6. The separation of the density maxima of the two neutron stars as a function of time for the three Models H, O, and o.

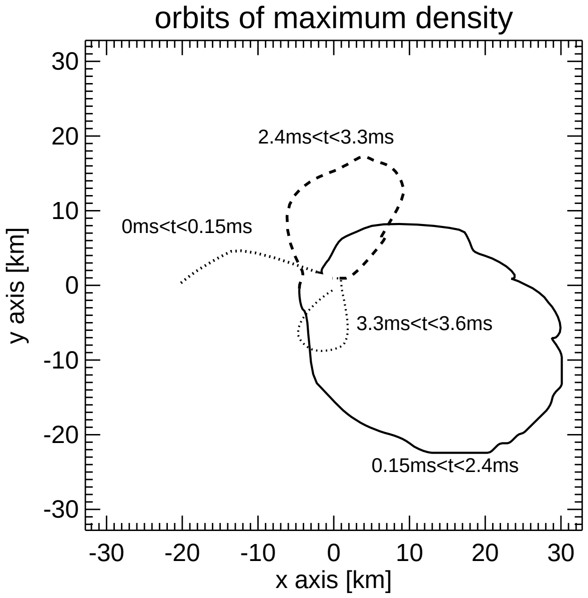

Fig. 7. Trajectory described by the density maximum of one of the neutron stars in a Eulerian frame for the off-center collision, Model O. Different line styles denote different orbits or phases between closest approaches. The kinks are numerical and due to the fact that the position of the maximum density is given by the integers corresponding to the indices of the numerical grid cells.

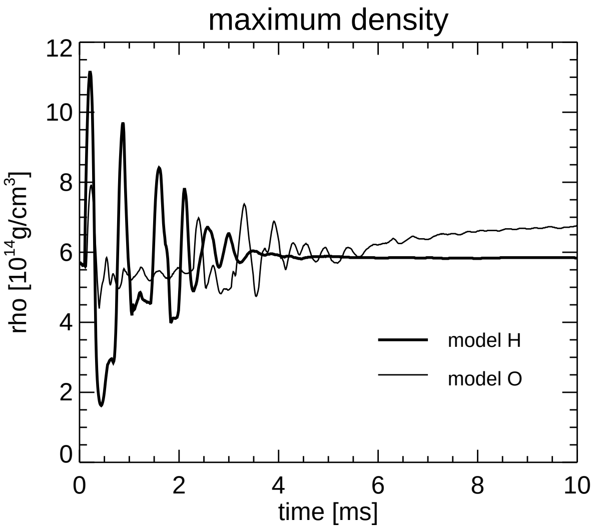

Fig. 8. The maximum density on the grid as a function of time for the two Models H and O.

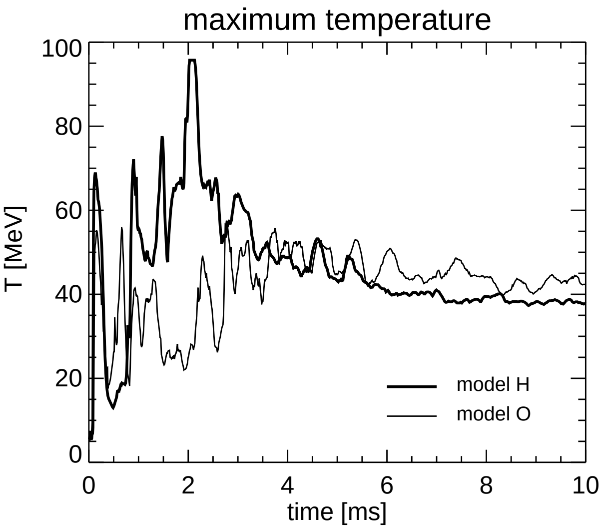

Fig. 9. The maximum temperature on the grid as a function of time for the two Models H and O.

violent oscillations until all the kinetic energy is dissipated into heat. The reexpansions produce peaks of the separation of the density maxima in Fig. 6, while the compression phases are reflected in a sequence of very large density maxima in Fig. 8 and temperature maxima in Fig. 9. The steady decrease of the density maxima in Fig. 8 indicates that the oscillations come to a rest within about 4 ms. In contrast, the maximum temperature increases from one compression to the next (Fig. 9) because of the dissipative heating of the stellar plasma. The most extreme temperatures that are reached in Model H during the dynamical phase, $0 < t \lesssim 4\,\mathrm{ms}$, are close to 100 MeV. After settling into a static state $t > 4\,\mathrm{ms}$, the maximum temperatures in the collision remnant is around 40–50 MeV.

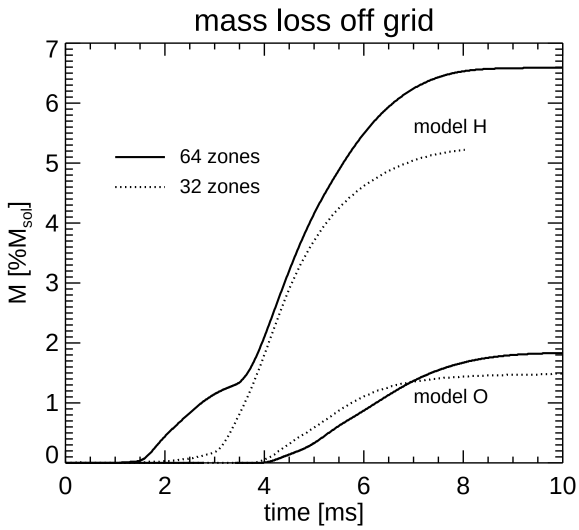

Fig. 10. Cumulative amount of matter flowing off the numerical grid (measured in $10^{-2}\,M_{\odot}$) as a function of time from the beginning of the simulations.

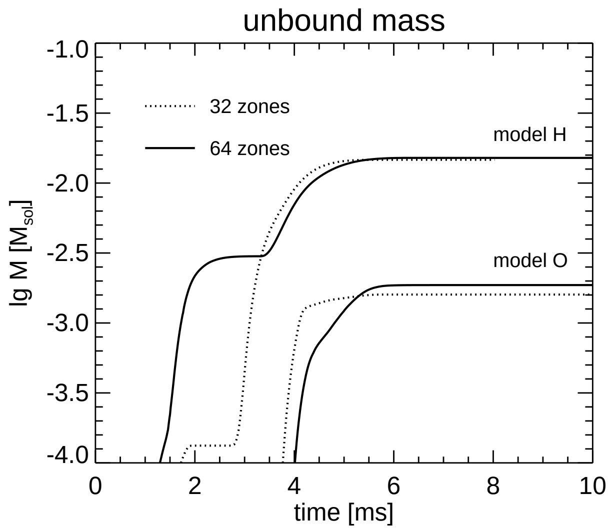

Fig. 11. Cumulative amount of matter that is unbound when it leaves the numerical grid (in units of $M_{\odot}$, plotted logarithmically) as a function of time for Models o, O, h, and H. The unbound mass is determined by the criterion that the sum of the specific gravitational, kinetic, and internal energies is positive.

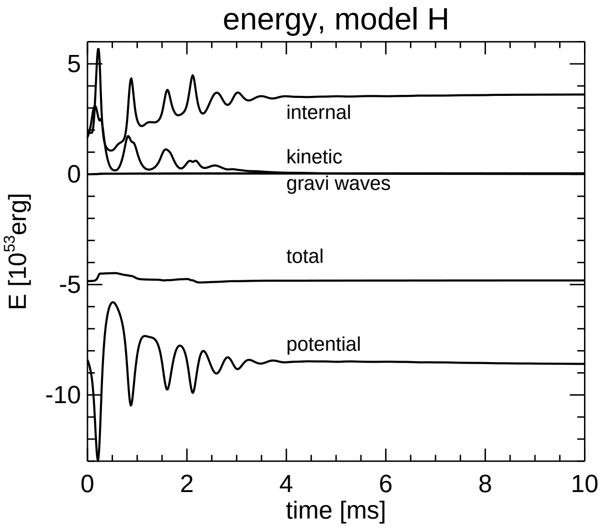

Fig. 12. The internal, kinetic, and potential energies of the matter on the grid and the sum of these energies as functions of time for Model H. Also plotted is the cumulative energy carried away in gravitational waves.

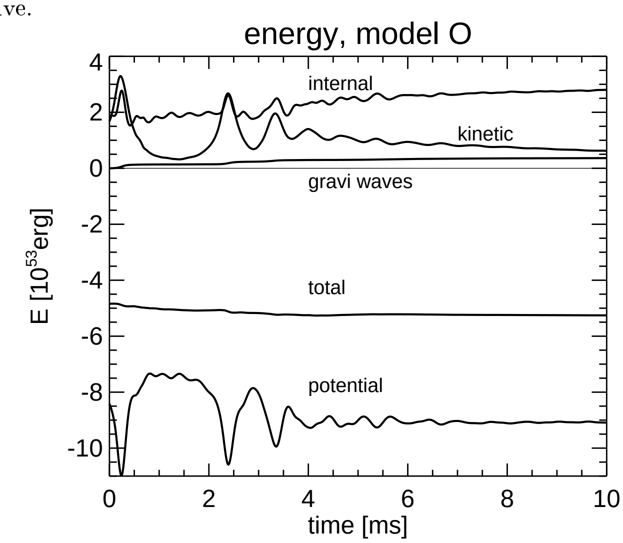

Fig. 13. Same as Fig. 12 but for Model O. The thin solid line marks the $E = 0$ level.

3.2. Off-center collision

The motion of the two neutron stars is rather complicated in case of the *off-center* collision, Model O. The first phase of the infall ($t \lesssim 0.1$ ms) proceeds essentially along point-mass binary orbits (Fig. 7), until the stars start to touch and orbital energy and angular momentum are converted into neutron star spin and are consumed by the acceleration of matter which is flung off the neutron star surfaces. The corresponding loss of orbital angular momentum and kinetic energy leads to a transformation of the initially parabolic orbits into elliptic ones. Even more orbital energy is transfered to internal energy when the neutron stars come into contact and inelastic interaction sets in.

After the first closest approach, visible in Fig. 6 as minimum distance $d_{\rm min} \approx 3$ km of the density maxima of the two neutron stars at $t \approx 0.15$ ms, the positions of the density maxima describe three nearly elliptic orbits between moments of closest approach at $t \approx 0.15\,\mathrm{ms}$, 2.4 ms, 3.3 ms, and 3.6 ms (see also Fig. 6). In Fig. 7 these three orbits, represented by the x-y-trajectory of the density maximum of one of the neutron stars, are discerned by different line styles. The diameters of the orbits (and thus the maximum separation of the density maxima) become successively smaller due to the inelasticity of the contact between the stars during their close encounters. The major axis of the first ellipse has a length of more than 30 km, corresponding to an apastron separation of the density maxima on the grid of about 65 km at $t \approx 1.2\,\mathrm{ms}$ (Fig. 6), much larger than the initial distance of the neutron star centers which was 42 km. This means that the neutron stars separate again after their first encounter, but fall back towards each other again. Even during the second apastron at $t \approx 2.9\,\mathrm{ms}$, the density maxima of the two stars have a distance of about 35 km, which is larger than the sum of their initial radii $2R_{\mathrm{ns,i}} = 30\,\mathrm{km}$. During the third and the subsequent quasi-elliptic orbits the neutron stars are not able to separate again. While the first bound orbit has a period of about 2.2 ms, the second, smaller one has only $\sim 0.9\,\mathrm{ms}$, and the following are even shorter (Figs 6 and 7).

In Figs. 3 and 4 the density distribution, temperature, electron fraction, and entropy per nucleon are plotted for Model O in the orbital plane at two different stages during the off-center collision. The left panels show the results for a time close to the apastron of the first orbital ellipse, i.e., a little more than a millisecond after the first closest approach. The neutron stars are tidally strongly deformed and gas has been swept into the surroundings during the first direct contact and interaction (Fig. 3a). There is a dense gas bridge ($\rho \sim 10^{12}$–$10^{13}\,\mathrm{g\,cm^{-3}}$) between the stars which continue to wobble and oscillate along their orbits. The temperature has climbed to nearly 40 MeV in distinct hot spots where the gas bridge hits the denser cores of the stars (Figs. 3c and 9), whereas the extended cloud of gas surrounding the orbiting bodies has a temperature of 1–5 MeV. In this ambient gas, $\bar{\nu}_e$ production by positron capture onto neutrons has raised the electron fraction from initially less than about 0.05 to maximum values around 0.2 (Fig. 4a). The maximum entropy values of $s \sim 11\,k$ per nucleon are produced by bow shocks in front of the rather dilute ($\rho \sim 10^{9}$–$10^{10}\,\mathrm{g\,cm^{-3}}$) clouds reaching outward from the two neutron stars. Clumps of gas with entropy $s \sim 5$–$6\,k$/nucleon are scattered in the surroundings of the collision site. Note that in contrast to the head-on collision, there is no shock heating of the interior of the neutron stars. Up to the end of the simulation the high-density cores of the neutron stars retain their low initial entropy, even after they have merged into one body.

The right panels in Figs. 3 and 4 show snapshots at a time near the end of the simulation ($t = 9.27\,\mathrm{ms}$). The distributions of density, entropy, and electron fraction have become roughly circular in the x-y-plane: A compact, dense central body ($\rho > 10^{12}\,\mathrm{g\,cm^{-3}}$) with $T \sim 5$–$10\,\mathrm{MeV}$ (outside of two distinct hot spots where $T \sim 40\,\mathrm{MeV}$), $Y_e \sim 0.04$–0.1, and $s \lesssim 7\,k$/nucleon is surrounded by an extended envelope with somewhat larger Y_e and s (but lower temperature), which is rapidly rotating and which is stabilized by centrifugal forces. Therefore the vertical extension of the gas envelope is significantly smaller than its diameter in the orbital plane; the density contour corresponding to $\rho = 10^{10}\,\mathrm{g\,cm^{-3}}$ extends to a radius of about 130 km in the orbital plane, whereas its butterfly shape has a maximum vertical height of roughly 70 km (Fig. 5). Even the compact core is rotationally deformed with an axis ratio of 1:1.5. Nevertheless, there is a considerable amount of gas at large heights $|z|$ above and below the orbital plane. By spatial integration we find $3.8 \times 10^{-2}\,M_\odot$ for $|z| \geq 40\,\mathrm{km}$, $2.2 \times 10^{-2}\,M_\odot$ for $|z| \geq 50\,\mathrm{km}$, and still $6.0 \times 10^{-3}\,M_\odot$ for $|z| \geq 80\,\mathrm{km}$.

3.3. Comparison of head-on and off-center collisions

The different dynamical evolutions of the head-on collision, Model H, and the off-center collision, Model O, are reflected in the different time histories of the maximum density (Fig. 8) and the maximum temperature (Fig. 9) on the grid. Model H shows very large amplitudes of the maximum density at the moments of strongest compression with up to a factor of ~ 10 larger values compared to the return points of expansion phases. These density fluctuations are damped in a sequence of 5–6 strong oscillations, and a stationary value is reached after about 4 ms. The temperature evolution reveals spikes and valleys, respectively, at the same moments, but there is a general trend of the temperature to increase during the dissipative oscillatory compressions and reexpansions. Although in Model O the variations of the separation of the density maxima are much more pronounced than in Model H (Fig. 6), the maximum density and temperature on the grid show much less extreme fluctuations because the neutrons stars describe orbits around each other and do not crash violently into each other. One can recognize peaks of the maximum density correlated with the moments of closest approaches, $t \approx 0.15\,\mathrm{ms}$, 2.4 ms, 3.3 ms, and 3.6 ms (compare Fig. 8 and Fig. 7). The whole evolution of Model O is much less violent than that of Model H. Nevertheless, on a longer timescale $t \gtrsim 4\,\mathrm{ms}$, both models settle to roughly the same maximum temperature of 40–50 MeV. The maximum density in Model O becomes even somewhat larger than in Model H, because the latter has been heated to higher entropies and therefore thermal pressure causes an expansion of the collision remnant. In addition, the compact core of the remnant of Model H is less massive as a result of the larger mass loss during the collision.

The more violent collision and therefore higher temperatures in Model H push more matter off the grid than

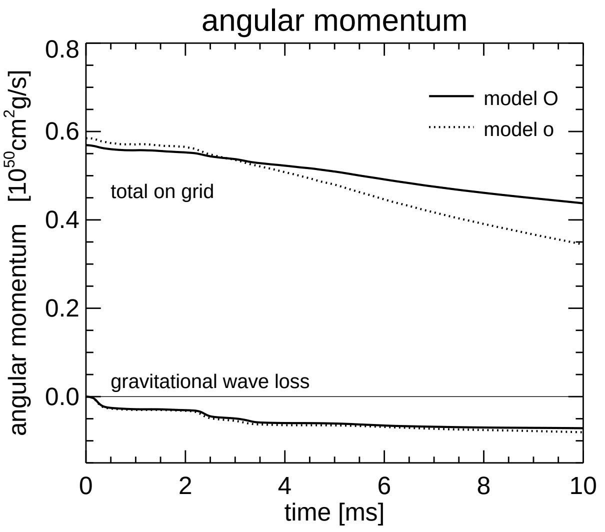

Fig. 14. Total angular momentum (z-component) of the matter on the grid (upper curves) and cumulative angular momentum loss by gravitational wave emission (lower curves) as functions of time for Models O and o. Gravitational waves carry away about 13% of the initial angular momentum of the colliding neutron stars and another non-negligible amount ($\sim 3.5\%$) is taken away by the matter flowing off the numerical grid.

in Model O (Fig. 10). Also a larger fraction of this matter gets unbound (Fig. 11) which is the case when the total specific energy of the gas, defined as the sum of the specific kinetic, internal, and gravitational potential energies, becomes positive. In Model H about $1.5 \times 10^{-2}\,M_\odot$ are able to escape the gravitational potential of the collision remnant, whereas it is little more than one tenth of this amount in Model O (cf. Table 1). Obviously, the angular momentum of Model O (see Fig. 14) and the associated centrifugal shredding of material can hardly compete with the ejection of gas in the strong shock waves occurring in Model H. We note in passing that Rasio & Shapiro (1992) (RS) found a significantly larger amount of mass loss (up to about 5% of the total mass) in their simulations of head-on collisions between two identical $\gamma = 2$ polytropes, compared to only $\sim 0.46\%$ that can escape from the system in our Model H. The difference is presumably caused by a combination of reasons, the use of different equations of state and correspondingly different stellar structure and mass (Lattimer & Swesty nuclear EOS here vs. $\gamma = 2$ adiabatic EOS by RS), the inclusion of gravitational wave back-reaction on the hydrodynamical flow in our simulations, and last but not least the use of different numerical schemes (Eulerian PPM here vs. SPH by RS) in combination with possibly different criteria to determine the unbound mass.

The temporal evolutions of the internal, kinetic, and gravitational potential energies (Figs. 12 and 13) show structures that correspond to the stages of the dynamical interactions of the colliding stars. The internal energy of Model H oscillates strongly with maxima at the moments of strongest compression (compare Figs. 8 and 12) which coincide with maxima of the kinetic and minima of the potential energy. There is a general trend for the internal energy to increase with time. This corresponds to a decrease of the kinetic energy (while the potential energy fluctuates around an essentially constant level) and thus reflects the action of dissipative forces. In the off-center collision of Model O the kinetic energy is much less efficiently converted into internal energy. The latter exhibits a continuous increase with superimposed, but much less dramatic, local peaks at the instants of closest approach, also coinciding with maxima of the kinetic and minima of the potential energy. This reflects the dynamical transformation between the different energy forms. Near the end of the computed evolution, practically all of the kinetic energy of Model O is rotational energy, $E_{\rm kin} = E_{\rm rot}$. Using the values from Fig. 13, we determine the following ratio of kinetic energy to the gravitational binding energy: $\beta = E_{\rm kin}/E_{\rm rot} \approx 0.08$.

The total energies of Model H and Model O (defined as the sum of kinetic, internal, and potential energies of all gas on the grid) are also shown in Figs. 12 and 13, respectively. In Model H minor variations of the total energy between $t \approx 0.2\,$ms and $t \approx 2.2\,$ms are numerical because of the extremely violent collision. Since the energy carried away by gravitational waves and mass loss off the numerical grid is negligible, the total energy at the beginning and end of the simulation are nearly equal. In contrast, in Model O the energy emitted in gravitational waves leads to a gradual decrease of the total energy of the gas on the grid.

Fig. 14 shows the total angular momentum (z-component) of the gas on the grid and the cumulative value of the angular momentum carried away by the emitted gravitational waves as a function of time for Models O and o. There is very good agreement of both calculations concerning the angular momentum loss in gravitational waves. This indicates that the overall mass distribution in the neutron stars (which enters the calculation of the mass quadrupole moment needed for the evaluation of the gravitational-wave source terms) is sufficiently well represented even on the coarser grid of Model o. Most of the decrease of the gas angular momentum is explained by the gravitational wave emission. An additional effect comes from the mass loss off the computational grid at $4\,{\rm ms} \lesssim t \lesssim 8\,{\rm ms}$ (Fig. 10) which removes an angular momentum of about $\Delta J_z \approx M_{\rm g} r_{\rm g} v_{\rm g} \approx 2 \times 10^{48}\,{\rm g\,cm^2\,s^{-1}}$ (with $M_{\rm g}$ taken from Table 1 and $r_{\rm g} \approx 160\,$km being the grid radius and $v_{\rm g} \approx 3.5 \times 10^9\,{\rm cm\,s^{-1}}$ the nearly tangential velocity of the gas when it leaves the grid) or 3.5% of the initial angular momentum. However, although the gravitational wave loss and the mass flowing off the grid are very similar in both models, Model o exhibits a steeper decrease of the total angular momentum at $t \gtrsim 3\,$ms than Model O. This difference is purely numerical and caused by the coarser grid resolution of Model o. Even in the better resolved calculation, Model O, about 7% of the initial angular momentum are destroyed by numerical effects at the end of the simulation.

The relativistic rotation parameter is defined as $a \equiv Jc/(GM_{\rm tot}^2)$ where $M_{\rm tot}$ is the total mass of the system ($M_{\rm tot} = 2M$ initially with M being the mass of one of the neutron stars) and J is the total angular momentum relative to the center of mass. We have an initial value of $a = 0.60$ and find a value of $a \gtrsim 0.47$ (in Model O) at the end of the simulation after angular momentum has been removed from the system by gravitational waves and ejected matter. Since $a < 1$ rotation seems unable to prevent the collapse of the collision remnant to a black hole if the remnant mass exceeds the maximum stable mass of the employed equation of state (see also RJS and Rasio & Shapiro, 1992, and references therein). Thermal pressure can increase this stable mass limit only insignificantly (cf. Goussard et al. 1997) and, if so, only during the transient period of neutrino cooling (note that the interior of the neutron stars retains its initial low entropy in the off-center collision, see Figs. 4c and d, and thus the temperature remains fairly low), and also rotation leads to an increase of the upper stability limit on the baryon mass by only $\lesssim 20\%$ (Friedman et al. 1986; Friedman & Ipser 1987).

4. Gravitational waves

The gravitational-wave luminosities and the cumulative energy loss in gravitational waves as functions of time for Models H and h and Models O and o are shown in Figs. 15 and 16, respectively, and the corresponding gravitational waveforms h_+ and $h_\times$ for Models H and O are plotted in Fig. 19.

In Model H the most prominent luminosity spike is created at the moment when the two neutron stars crash into each other and the gas flow is abruptly decelerated and redirected by the recoil shocks ($t \approx 0.22$ ms, cf. Fig. 1) which leads to a rapid change of the mass quadrupole moment. The peak luminosity reaches about 3.7×10^{55} erg/s (see also Fig. 17). A precursor with about 1/4 of the maximum luminosity is caused by the increasing tidal deformation of the neutron stars as they approach each other. After this initial outburst the gravitational-wave luminosity continues to oscillate regularly with a period between two maxima of roughly half a millisecond but with peaks at least one order of magnitude below the maximum luminosity. This indicates that the bulk of the matter quickly adopts a more or less spherical distribution. Within about 8 ms the luminosity falls by more than 5 orders of magnitude to less than 10^{50} erg/s. This dramatic drop is reflected in the gravitational waveforms of Model H which indicate that after $\sim$ 4 ms the activity has essentially ceased. This coincides with the complete dissipation of the kinetic energy at that time (see Fig. 12). More than 50% of the total energy emitted in gravitational waves are contained in the luminosity spike and after about 3 ms only insignificant further contributions are added (cf. cumulative energy loss in Fig. 15). From Figs. 15 and 17 one learns that the coarser resolution of Model h leads only to minor differences compared to Models H and $\mathcal{H}$ with the tendency to overestimate the gravitational-wave luminosity and emitted energy. Models H and $\mathcal{H}$ are hardly distinguishable in Fig. 17 and the computations seem to be converged.

Model O is an approximately ten times more energetic source of gravitational waves than Model H and emits a total energy of $2 \times 10^{-2}\, M_\odot c^2$. On the one hand the first luminosity maximum at $t \approx 0.22$ ms is nearly twice as high ($\sim 6 \times 10^{55}$ erg/s) as in Model H and nearly four times longer (half width about 0.2 ms compared to 0.05 ms) (Fig. 18) On the other hand Model O continues its strong emission of gravitational waves for the whole computation period of 10 ms during which the luminosity on average stays around 10^{54} erg/s and hardly ever drops below 10^{53} erg/s. This can be explained by the rapid change of the quadrupole moment of the system as the two neutron stars repeatedly come close and separate again on their quasi-elliptic orbits around each other (cf. Fig. 7) and by the large kinetic energy retained as rotational energy of the collision remnant at the end of the simulation (Fig. 13). Several peaks of the gravitational-wave luminosity can be correlated with the moments of closest approach of the density maxima of the two neutron stars (compare Figs. 16 and 6), and two strong, short minima of the luminosity (at $t \approx 1.2$ ms and $t \approx 4.1$ ms) coincide with instants of maximal separation. In Model O only about 30% of the total energy emitted in gravitational waves is contained in the first luminosity spike, another $\sim 50\%$ are added during the second and third periastrons ($t \approx 2.4$ ms and $t \approx 3.3$ ms), and a non-negligible fraction ($\sim 20\%$) comes at later times. The waveforms of Model O (Fig. 19) exhibit a rather irregular structure during the first 4–5 ms of the evolution with a peak amplitude at $t \approx 0.22$ ms which is about twice as high as in Model H. They continue with a very regular, slowly damped sinusoidal modulation until the end of the simulation at $t \approx 10$ ms.

Finally, in Figs. 17 and 18 we compare the first large spike of the gravitational-wave luminosity with the corresponding results obtained by Centrella & McMillan (1993) and Rasio & Shapiro (1992). In order to do that we rescale and renormalize their dimensionless quantities to physical units for our chosen neutron star parameters by using the dynamical timescale

$$t_{\rm D} \equiv \left(\frac{R^3}{GM}\right)^{1/2} \approx 0.125 \text{ ms} \tag{7}$$

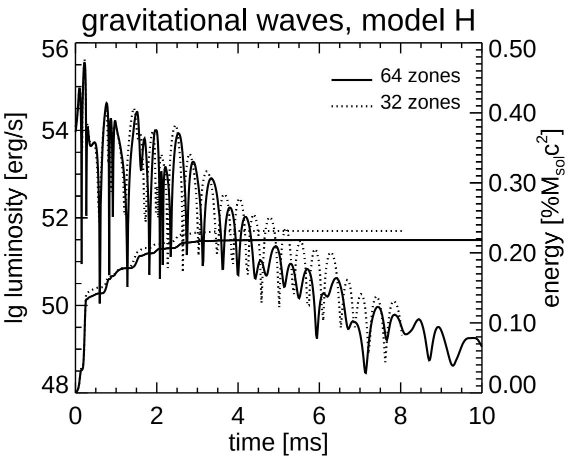

Fig. 15. Gravitational-wave luminosity and cumulative energy emitted in gravitational waves (measured in units of $10^{-2}\,M_\odot c^2$) as functions of time for Models H and h.

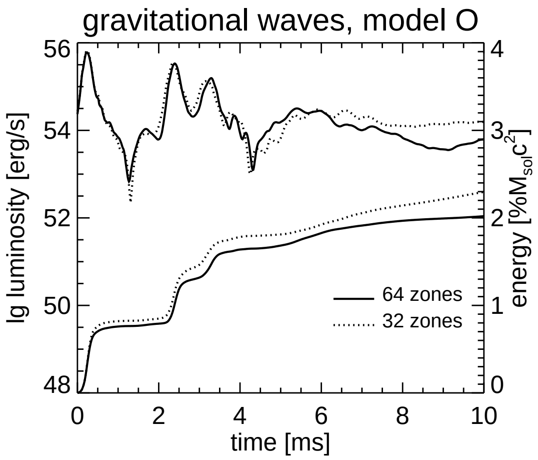

Fig. 16. Same as Fig. 15 but for Models O and o.

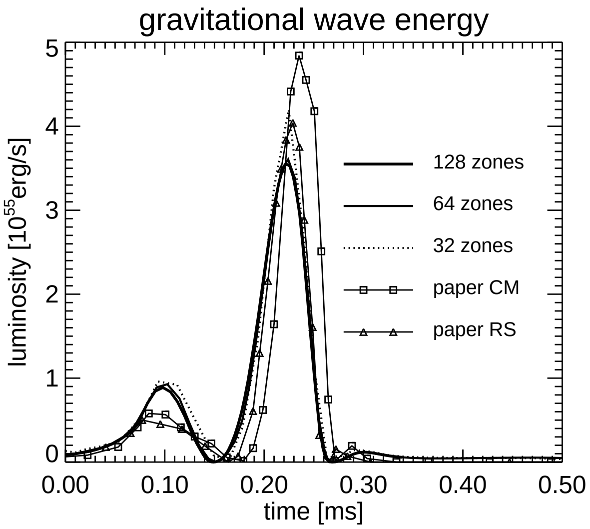

Fig. 17. Gravitational-wave luminosity as a function of time for the *head-on* collision Models $\mathcal{H}$, H and h, compared with the results from Centrella & McMillan (CM, 1993, Fig. 8) and from Rasio & Shapiro (RS, 1992, Fig. 9).

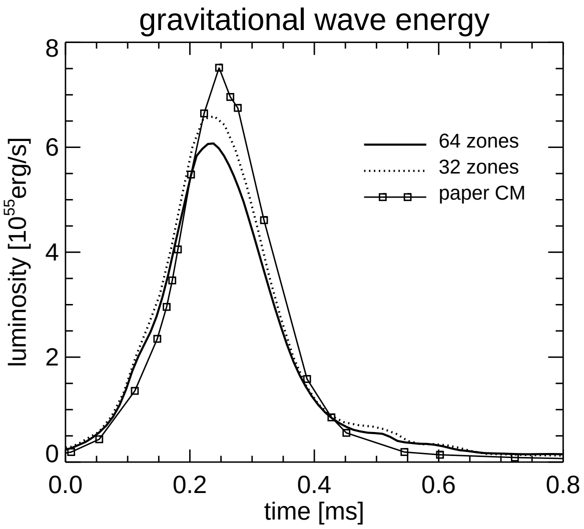

Fig. 18. Gravitational-wave luminosity as a function of time for the *off-center* collision Models O and o, compared with the result from Centrella & McMillan (CM, 1993, Fig. 11).

with $M = 1.63\,M_\odot$ as the mass and $R = 15\,$km as the radius of the neutron stars, and by the scaling the luminosity with the factor

$$L_0 \equiv \frac{1}{G}\left(\frac{GM}{cR}\right)^5 \approx 3.86\cdot 10^{55}\ \mathrm{erg/s}\,. \tag{8}$$

Moreover, there is a time shift between their calculations and ours because of the different initial center-to-center distances of the neutron stars. While it was $a_0 = 42\,$km in our models, Rasio & Shapiro (1992) and Centrella & McMillan (1993) assumed $a_1 = 4R = 60\,$km for their head-on collisions, and Centrella & McMillan (1993) took $a_1 \approx 4.53R \approx 68\,$km for the off-center case. The time lag for the parabolic infall trajectories of the two masses with different initial separations can be determined as the difference of the times to reach the minimum distance (periastron), to be (Roy, 1982, Eqs. (4.82) and (4.85))

$$\Delta t = \frac{\sqrt{2}(A_1 - A_0)}{3\sqrt{GM_\mathrm{t}}} \tag{9}$$

with $A_i \equiv (a_i + 2R_\mathrm{p})\sqrt{a_i - R_\mathrm{p}}$ $(i = 0, 1)$. $M_\mathrm{t} = M_1 + M_2 = 2M$ is the total mass of the system and the periastron distance R_p is the separation of two point particles

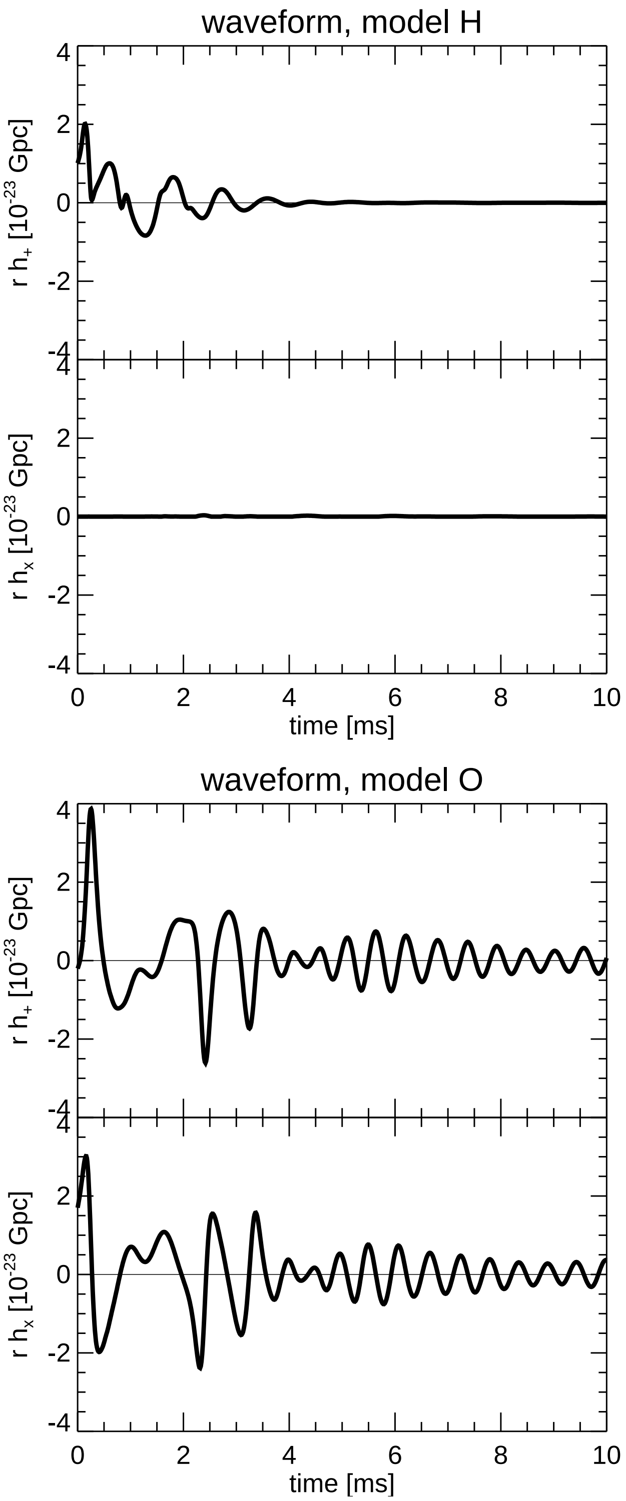

Fig. 19. Gravitational waveforms, h_+ and $h_\times$, for Models H and O, respectively, as functions of time. Note that the gravitational-wave field $h_\times$ with the cross polarization is practically zero in case of the head-on collision, Model H, because there are only very small deviations from the mirror symmetry relative to the y-z plane when the hot contact layer of the two neutron stars becomes unstable against shear motions (compare Figs. 1 and 2).

of mass M at closest approach, which is set to zero for the head-on collision and to $R_\mathrm{p} = 1R$ for the off-center case.

Taking into account these aspects in Figs. 17 and 18, we find good overall agreement between the gravitational-wave luminosities from the different calculations, both in shape and magnitude. The remaining minor discrepancies can be attributed to the use of the Lattimer & Swesty (1991) EOS in our calculations instead of an adiabatic EOS with constant index $\gamma = 2$, the possible influence from the inclusion of gravitational-wave back-reactions in our models, and the effects resulting from different numerical schemes and different resolution.

5. Neutrino emission

Because of the different dynamical evolution, the head-on and off-center collisions also show distinctive differences in the neutrino emission. The total neutrino luminosities for Models H and h and Models O and o as functions of time are plotted in Fig. 20.

One can see that in the head-on collision (Models H and h) a first very luminous burst of neutrinos with a peak flux of more than 5×10^{53} erg/s is produced at the moment when the two stars crash into each other and the neutron star matter is shock heated and hot gas is squeezed out perpendicular to the collision axis (see Fig. 1a and c). A second and third luminosity maximum, however, with about 8 times larger peak fluxes of more than 4×10^{54} erg/s are present in the time interval $1.5\,\mathrm{ms} \lesssim t \lesssim 3.5\,\mathrm{ms}$ which is the time of maximum temperatures in the collision remnant (Fig. 9) when the hot matter starts to expand and to spread out over a larger volume (Figs. 1b and 1d). A luminosity of $L_\nu = 4\times10^{54}\,\mathrm{erg/s} \approx 4\pi R_\nu^2 \frac{c}{4}(3\cdot\frac{7}{8}a_\mathrm{rad}T_\nu^4)$ corresponds to a neutrinosphere with radius $R_\nu \approx 50\,\mathrm{km}$ which radiates neutrinos and antineutrinos of all flavors as black body with temperature $T_\nu \approx 8.5\,\mathrm{MeV}$. Figures 1b and d confirm that the massive, nearly spherical central body of the collision remnant, which is embedded in a cloud of less dense and cooler gas, has a radial size and "surface" temperature in this estimated range. The duration of this extremely luminous burst is only about 2 ms, after which the total luminosity settles down to a much lower but still sizable value around 10^{54} erg/s. During the ~ 10 ms of simulation time, Models H and h emit an energy of $6.7\times10^{-3}\,M_\odot c^2$ or $1.2\cdot10^{52}$ erg in neutrinos, of which 50% are radiated during the double peak of the luminosity. Model H is a stronger source of neutrinos than of gravitational waves; the latter carry away only about $2.2\times10^{-3}\,M_\odot c^2$ (Fig. 24). Nevertheless, despite of the extremely high luminosity the total energy radiated in neutrinos by Model H is still one order of magnitude below the estimates by Katz & Canel (1996).

During the break-out of the bounce shock at $t \approx 0.2$ ms neutrinos with average energies in excess of 50 MeV are emitted from Model H (Fig. 21). A second phase of very

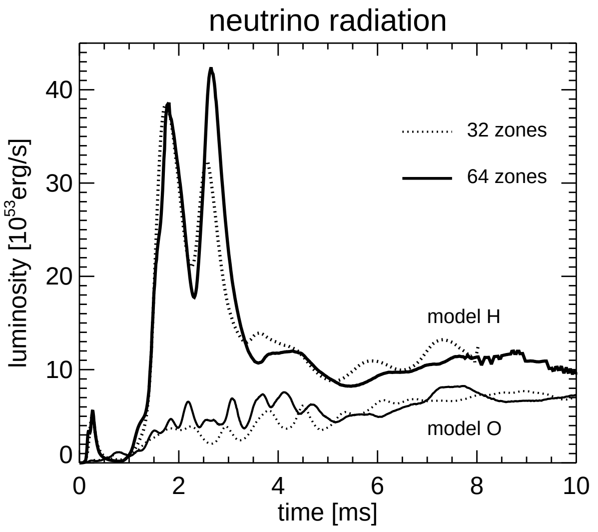

Fig. 20. Total neutrino luminosities (sums of the contributions from all neutrino and antineutrino flavors) as functions of time for Models H and h and Models O and o.

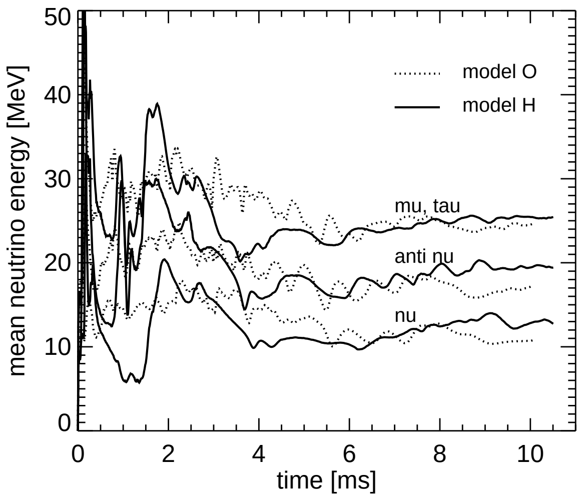

Fig. 21. Average energies of emitted neutrinos ν_e, $\bar{\nu}_e$, and ν_x ($\equiv \nu_\mu$, $\bar{\nu}_\mu$, ν_τ, $\bar{\nu}_\tau$) as functions of time for Models H and O.

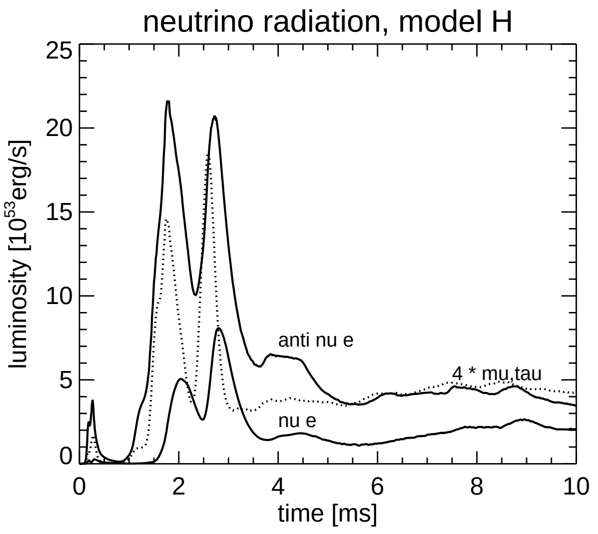

Fig. 22. Luminosities of the individual neutrino and antineutrino flavors (ν_e, $\bar{\nu}_e$, and the sum of all ν_x) as functions of time for Model H.

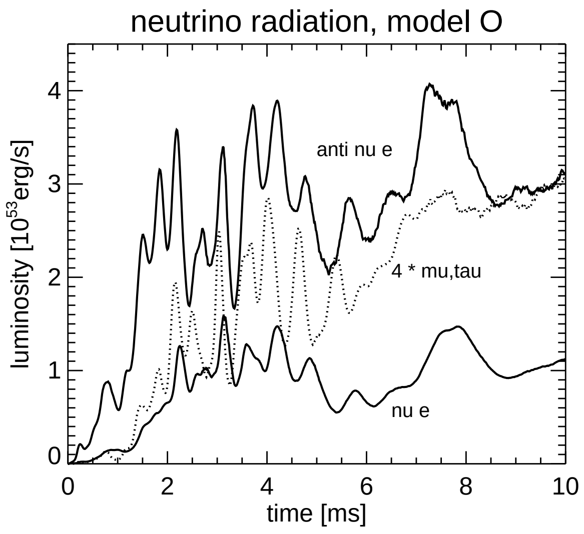

Fig. 23. Same as Fig. 22 but for Model O.

high mean energies coincides with the two luminosity spikes and therefore the phase of highest temperatures in Model H. As is well known from type II supernovae (see, e.g., Janka 1993), neutron-rich, hot neutron star matter is more opaque to ν_e than to $\bar{\nu}_e$ because of frequent captures of the ν_e on the abundant free neutrons. Heavy-lepton neutrinos ($\nu_x \equiv \nu_\mu$, $\bar{\nu}_\mu$, ν_τ, $\bar{\nu}_\tau$) are even less strongly coupled to the stellar medium since their opacity is dominated by neutral-current neutrino-nucleon scatterings but they do not interact with nucleons via charged-current reactions. For these reasons $\bar{\nu}_e$ decouple energetically from the hot plasma at higher densities and thus usually higher temperatures than ν_e, and ν_x at even higher densities and temperatures. This explains why typically the mean energy of the emitted ν_e is lower than that of $\bar{\nu}_e$ which in turn is below the average energy of ν_x (see Fig. 21). After $t \gtrsim 4\,$ms we obtain mean energies of $\langle\epsilon_{\nu_e}\rangle \approx 10$–$13\,$MeV, $\langle\epsilon_{\bar{\nu}_e}\rangle \approx 15$–$20\,$MeV, and $\langle\epsilon_{\nu_x}\rangle \approx 20$–$25\,$MeV which is in the range of values found during the neutrino cooling phase of newly formed neutron stars in type II supernovae. De-

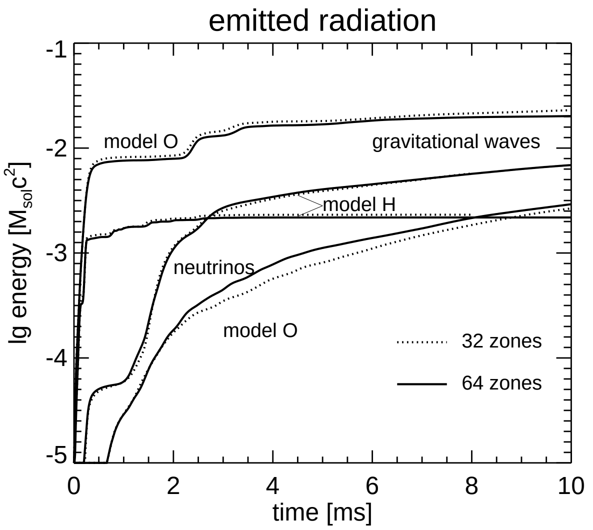

Fig. 24. Comparison of the cumulative energies emitted in neutrinos and gravitational waves (in units of $M_{\odot}c^2$) as functions of time for the four Models H, h, O, and o.

spite of this generic ranking of the mean energies, the ν_e luminosity of the collision remnant is larger than the luminosity in each individual type of ν_x, and the $\bar{\nu}_e$ luminosity of the neutron-rich, hot neutron star matter dominates the ν_e luminosity (Fig. 22). The difference in ranking between neutrino luminosities and mean energies of emitted neutrinos reflects the fact that the emission is not like an ideal black-body, but non-equilibrium effects play a role. Moreover, Fig. 25 shows that there is an extended region (with a broad range of temperatures and densities) where the neutrino fluxes are fed by local neutrino energy losses. Therefore the neutrino emission can hardly be characterized by the conditions of thermodynamical equilibrium at a well defined neutrino emitting surface ("neutrinosphere") associated with each type of neutrino or antineutrino.

In the off-center collision, Models O and o, the neutrino luminosity reveals a steady increase and does not have such pronounced maxima as seen in Model H (Fig. 20), although some fluctuations up to a factor of 2 are present. At the end of our simulations ($t \approx 10\,\mathrm{ms}$), Model O has a total neutrino luminosity of about $7 \times 10^{53}\,\mathrm{erg/s}$ which is only 30% less than in Model H. Because of the lack of a phase of extremely high neutrino emission and the strong production of gravitational waves during its whole evolution, Model O loses only half the energy in neutrinos as Model H but is a much stronger gravitational-wave source (Fig. 24). A comparison of the two plots in Fig. 25 shows that in Model O the neutrino emitting gas cloud (at $t \approx 10\,\mathrm{ms}$) is more extended than in Model H (at $t \approx 2.5\,\mathrm{ms}$) but the peak values of the local energy loss rate in neutrinos are only around $3 \times 10^{32}\,\mathrm{erg\,cm^{-3}\,s^{-1}}$ in Model O whereas they are above $10^{34}\,\mathrm{erg\,cm^{-3}\,s^{-1}}$ in case of Model H. The mean energies of the emitted neutrinos (Fig. 21) are very similar in Models O and H, and also the relative contributions of the different neutrino types to the energy loss are roughly similar, as can be seen from a comparison of the relative sizes of the individual neutrino luminosities in Figs. 23 and 22.

6. Neutrino-antineutrino annihilation

The rate of energy deposition by neutrino-antineutrino annihilation increases, roughly, with the product of the local neutrino and antineutrino energy densities times the mean energy of these neutrinos times a factor that accounts for the angular distribution of the neutrinos (the process is very sensitive to the angle at which neutrinos and antineutrinos collide, for details, see RJST). In the spherically symmetric situation this can be converted into a product of the neutrino and antineutrino luminosities times the sum of the mean neutrino and antineutrino energies times a normalized factor which results from the phase space integration over the local neutrino distribution functions and which depends on the geometry of the considered problem. This was used to arrive at the approximate description summarized in Eqs. (1)–(6) of Sect. 2.2 employed here to evaluate Model H for the energy deposition by $\nu\bar{\nu}$ annihilation in the surroundings of the collision remnant.

Neutrino-antineutrino annihilation is considered as a mechanism to pump energy into a fireball consisting of e^+, e^-, photons, and a small number of baryons. This fireball was suggested to be a possible source of gamma-ray bursts from neutron star collisions at cosmological distances (see, e.g., Katz & Canel 1996) if the energy in the fireball is sufficiently large, $E_{\mathrm{fb}} \approx E_\gamma \approx E_{\mathrm{ann}} \gtrsim 10^{51}\delta\Omega/(4\pi)\,\mathrm{erg}$, and if the baryon loading of the fireball is sufficiently small, $M_{\mathrm{fb}} \lesssim 10^{-5}\,M_{\odot}$ (for a canonical energy $E_{\mathrm{fb}} \sim 10^{51}\,\mathrm{erg}$) so that the fireball can expand relativistically with a Lorentz factor $\Gamma_{\mathrm{fb}} = E_{\mathrm{fb}}/(M_{\mathrm{fb}}c^2) \gtrsim 100$. Two questions arise from this suggestion. First, is the conversion of neutrino-antineutrino energy into electron-positron pairs enough efficient to provide the desired energy, and, second, how large is the baryon mass contained in the fireball created through $\nu\bar{\nu}$ annihilation?

In the following we attempt to give answers to these two questions on grounds of our hydrodynamical collision models. Here we only report on the evaluation of the head-on collision Model H. We concentrate on this model for two reasons. On the one hand, the efficiency of $\nu\bar{\nu}$ annihilation increases strongly with the neutrino luminosities and with the mean energies of the emitted neutrinos. Therefore Model H with its larger neutrino emission appeared to us as the more interesting one. On the other hand, our simulations have demonstrated that even in the off-center collision the interaction of the two neutron stars is so dramatic that a lot of matter is ejected perpendicularly to the orbital plane. Therefore, despite of the large angular momentum in the system, the axis region is polluted

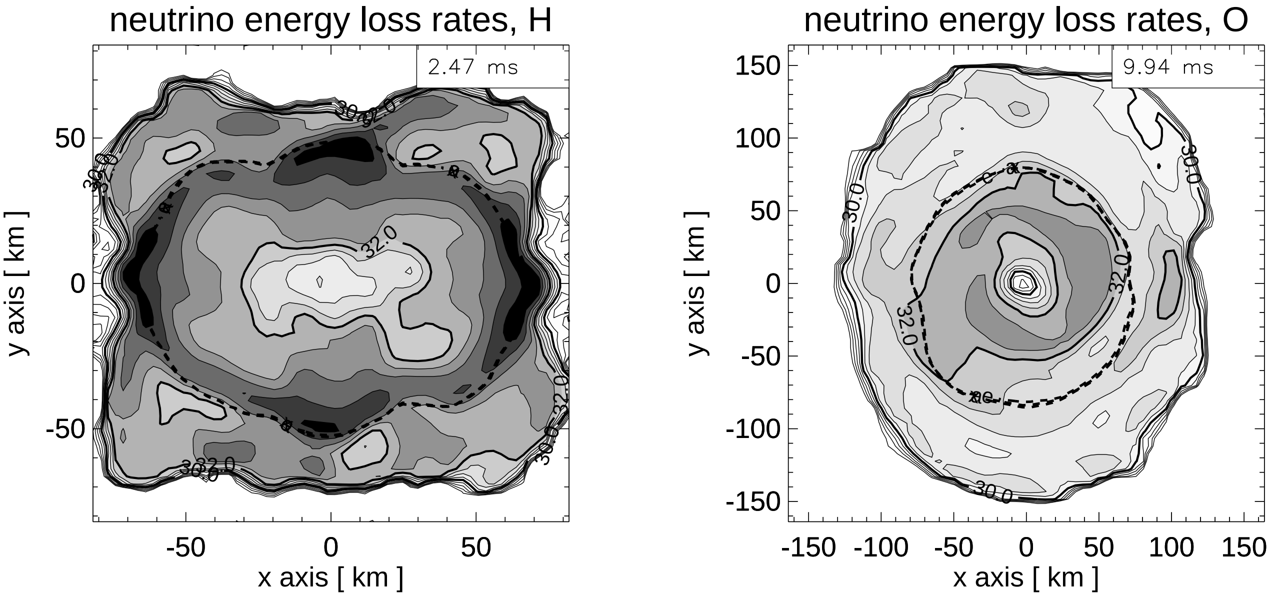

Fig. 25. Contour plots of the local energy loss rates due to the emission of neutrinos and antineutrinos of all flavors. The left plot shows a cut in the $z = 0$ plane for Model H at time $t = 2.47$ ms, the right plot displays a cut in the orbital plane of Model O at time $t = 9.94$ ms. Note that the visualized region is larger in the latter figure. The contours are spaced logarithmically in steps of 0.5 dex, the bold lines are labeled with their corresponding values in units $\mathrm{erg\,cm^{-3}\,s^{-1}}$. The dashed lines indicate the approximate positions of the neutrinospheres (defined where the optical depths for ν_e, $\bar\nu_e$, and ν_x, respectively, are approximately unity).

with baryons (see Fig. 5), and both the remnants of the head-on and off-center collisions adopt more or less spherical shapes after the dynamic interactions, with a central massive object being surrounded by a less dense, extended cloud of hot baryonic gas (Figs. 1 and 3). From this point of view Model O did not seem to offer better perspectives for the emergence of a relativistic fireball from a baryon-depleted region near the collided neutron stars.

Figure 26 gives a map of the energy deposition rate by $\nu\bar\nu$ annihilation into e^+e^- pairs (averaged over the azimuthal angle around the z-axis according to Eq. (1)) in the surroundings of the collision remnant in Model H at time $t = 3$ ms which is inside the double peak structure of the neutrino luminosity of Fig. 20. One can see that the highest energy deposition rates of the order of $3\times10^{30}\,\mathrm{erg\,cm^{-3}\,s^{-1}}$ to $10^{31}\,\mathrm{erg\,cm^{-3}\,s^{-1}}$ occur immediately outside the neutrinospheres but in layers with densities still above and around $10^{10}\,\mathrm{g\,cm^{-3}}$. At the displayed time, the integral energy deposition rate in matter with density below $10^{11}\,\mathrm{g\,cm^{-3}}$ (evaluated according to Eq. (2)) is $3.4\times10^{52}\,\mathrm{erg\,s^{-1}}$.

Since the neutrino luminosities and mean energies of the emitted neutrinos show significant variation during the computation time (see Figs. 20, 21, and 22), we compute the time integral of the energy deposition rate, Eq. (3), by employing the approximate treatment summarized in Eqs. (4)–(6). The phase between $t \approx 1.5$ ms and $t \approx 3.5$ ms has by far the highest neutrino luminosity and therefore yields the largest contribution to the time integral. For this reason we calculate the temporal average of the term $L_{\mathrm{ann}}(t)/\mathcal{F}^*(t)$ in Eq. (4) by summing over $N = 3$ time points in this interval: $t_1 = 2.47$ ms, $t_2 = 3.01$ ms, and $t_3 = 3.59$ ms. We obtain

$$\frac{1}{N}\sum_{i=1}^{N}\left(\frac{L_{\mathrm{ann}}(t_i)}{\mathcal{F}^*(t_i)}\right) \approx 2\times10^{-57}\,\mathrm{MeV^{-1}\,erg^{-1}\,s}\,. \qquad (10)$$

Because the three terms of the sum are different by less than a factor 2, we think that the splitting of the time integral of Eq. (3) which led to the approximate form of Eq. (4) was justified. Taking the data for the individual neutrino luminosities $L_{\nu_e}(t)$, $L_{\bar\nu_e}(t)$, and $L_{\nu_x}(t)$ (Fig. 22) and the average neutrino energies $\langle\epsilon_{\nu_e}(t)\rangle$, $\langle\epsilon_{\bar\nu_e}(t)\rangle$, and $\langle\epsilon_{\nu_x}(t)\rangle$ (Fig. 21), we further find

$$\int_0^{10\,\mathrm{ms}} \mathcal{F}^*(t)\,\mathrm{d}t \approx 5\times10^{106}\,\mathrm{MeV\,erg^2\,s^{-1}}\,. \qquad (11)$$

Multiplying the results of Eqs. (10) and (11) we end up with a total energy deposition of $E_{\mathrm{ann}} \approx 10^{50}$ erg within our simulation interval of 10 ms for Model H (see also Fig. 27). The corresponding average energy deposition rate by $\nu\bar\nu$ annihilation of $\sim 10^{52}\,\mathrm{erg\,s^{-1}}$ is very large and means a conversion efficiency of $\nu\bar\nu$ energy to e^+e^- pairs of the order of 1%. Most of this energy is liberated during the 2 ms interval between $t \approx 1.5$ ms and $t \approx 3.5$ ms after the start of the simulation because of the enormous neutrino luminosity shortly after the collision of the neutron stars.

The energy of approximately 10^{50} erg in e^+e^- pairs and photons is released nearly isotropically (Fig. 26) and is only one order of magnitude below the canonical fireball energy $E_{\mathrm{fb}} \approx E_\gamma \sim 10^{51}\delta\Omega/(4\pi)$ erg. It may therefore

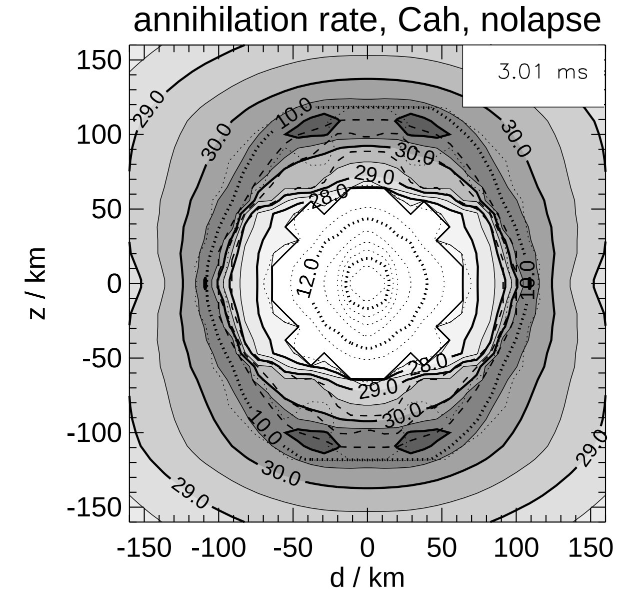

Fig. 26. Map of the local energy deposition rates (in $\mathrm{erg\,cm^{-3}\,s^{-1}}$) by $\nu\bar{\nu}$ annihilation into e^+e^- pairs in the vicinity of the merger for Model H at time $t = 3$ ms after the start of the simulation. The values are obtained as averages over the azimuthal angle around the z-axis, d measures the distance from the grid center in the x-y-plane. The corresponding solid contour lines are logarithmically spaced in steps of 0.5 dex, the grey shading emphasizes the levels with dark grey meaning high energy deposition rate. The dashed lines mark the (approximate) positions of the neutrinospheres of ν_e, $\bar{\nu}_e$, and ν_x (from outside inward), defined by the requirement that the optical depths in z-direction are $\tau_{z,\nu_i} = 1$. The dotted contours indicate levels of the azimuthally averaged density, also logarithmically spaced with intervals of 0.5 dex. The energy deposition rate was evaluated only in that region around the merged object, where the mass density is below $10^{11}\ \mathrm{g\,cm^{-3}}$. The integral value of the energy deposition rate at the displayed time is $3.4 \times 10^{52}\ \mathrm{erg\,s^{-1}}$.

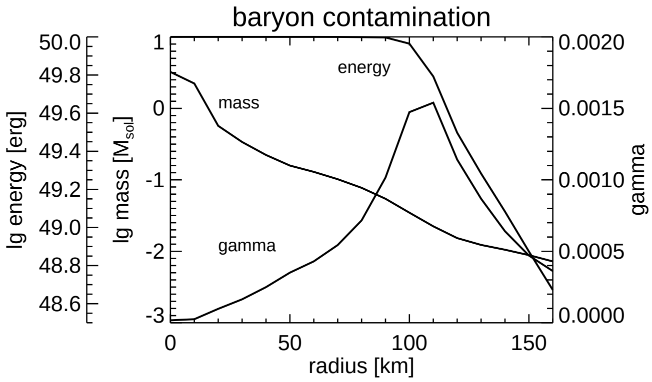

Fig. 27. Cumulative mass $M(r \geq R)$ and annihilation energy $E_{\nu\bar{\nu}}(r \geq R)$ outside of radius R, as functions of R for Model H at time 3 ms (same time as in Fig. 26). The corresponding relativistic Lorentz factor $\Gamma(R) \equiv E_{\nu\bar{\nu}}(r \geq R) / \left[M(r \geq R)c^2\right]$ is also plotted.

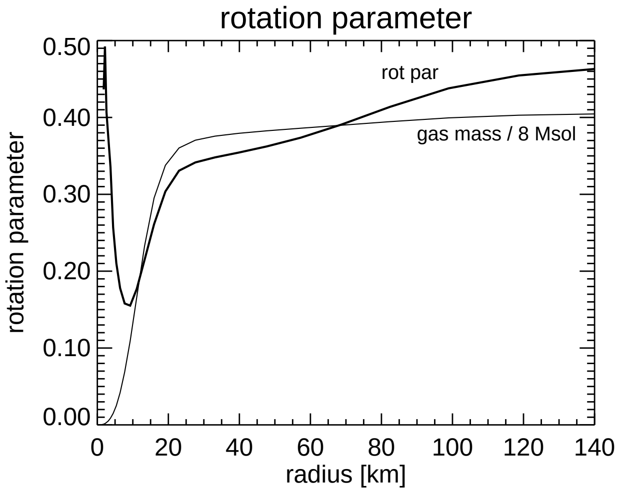

Fig. 28. The thick solid line gives the relativistic rotation parameter $a(r) \equiv J(r)c/(GM_{\mathrm{gas}}^2(r))$ for Model O as function of radius r. $J(r)$ is the angular momentum (in z-direction) inside r, $M_{\mathrm{gas}}(r)$ is the gas mass inside r which is plotted as thin solid line, given in units of $M_\odot$ and scaled down by a factor 8.

be sufficient to account for the shorter and weaker bursts whose energy is estimated to be typically more than a factor of 10 below the mean energy of the longer and more powerful bursts (Mao et al. 1994). However, most of the $\nu\bar{\nu}$ energy deposition happens very close to the neutrinospheres and thus in a high-density region (Fig. 26). Because of this, the baryon loading of the e^+e^--photon fireball is a serious problem. This is obvious from Fig. 27 where we give the energy from $\nu\bar{\nu}$-annihilation and the baryonic mass, integrated from outside inward to the radial position R given on the abscissa. In the region where 10^{50} erg are deposited, one has a baryon mass of $M \gtrsim 5 \times 10^{-2}\, M_\odot$ which is about 5 orders of magnitude too large to allow for highly relativistic expansion. The Lorentz factors which can be estimated as $\Gamma(R) \equiv E_{\nu\bar{\nu}}(r \geq R) / \left[M(r \geq R)c^2\right]$ are therefore around 10^{-3} instead of 100. For this reason, the huge and nearly isotropic baryon pollution of the $\nu\bar{\nu}$ energy deposition region seems to rule out the possibility that neutrinos from colliding neutron stars produce gamma-ray bursts.

7. Summary and discussion

We have reported results of three-dimensional Newtonian hydrodynamical simulations of the collision along parabolic orbits of two identical, non-rotating neutron stars with a baryonic mass of about $1.6\, M_\odot$. The simulations were done with a Eulerian PPM code, employing nested grids, using a physical nuclear EOS, and taking into account gravitational-wave emission and its back-reaction on the hydrodynamical flow as well as the emission of neutrinos from the heated neutron star matter. We have studied two different cases, each with varied resolution on the finest grid, a head-on collision and an off-center collision with a periastron distance of one stellar radius ($\approx$ 15 km). Our simulations allow us to draw the following main conclusions:

1.) *Dynamical evolution:* During the head-on collision of the two neutron stars, the collision remnant is heated by recoil shocks and the initial kinetic energy is efficiently shock-dissipated to thermal energy within a few violent pulsations on a timescale of about 3–4 ms, after which the collision remnant has an essentially spherical mass distribution. The neutron star matter is transiently heated to peak temperatures close to 100 MeV. Average temperatures are around 40–50 MeV, corresponding to entropies between $2\,k$/nucleon and $10\,k$/nucleon. The violent crash of the stars into each other leads to the dynamical ejection of about 0.5% of the system mass. In contrast, the off-center collision is much "milder" and the ejected mass is about a factor of 10 smaller, although the collision remnant retains a large fraction (about 30%) of the initial kinetic energy as rotational energy even after 10 ms at the end of our simulations. Only for extreme assumptions about the nuclear EOS will the $\gtrsim 3\,M_\odot$ remnant of the head-on collision not form a black hole on a dynamical timescale. We also believe that the remnant of the off-center collision will probably not be able to escape the collapse to a black hole within a few milliseconds. A mass of $3\,M_\odot$ is distributed within a radius of 30 km and $2.8\,M_\odot$ are within 20 km (Fig. 28) which is only about twice the Schwarzschild radius of a $3\,M_\odot$ black hole. Thermal pressure can only insignificantly raise the maximum stable mass of neutron stars (Goussard et al. 1997) and rotation is able to increase the stable mass limit by only $\lesssim 20\%$ (Friedman et al. 1986). The interior $\sim 2.8\,M_\odot$ of the remnant rotate nearly uniformly and the relativistic rotation parameter of this mass is only $a(r=20\,\mathrm{km}) = \left[Jc/(GM^2)\right]_{20\,\mathrm{km}} \approx 0.3$ (cf. Fig. 28), which is smaller than that of the maximally rotating, maximum-mass models constructed by Friedman et al. (1986). For all but one extreme EOS tested by Friedman et al. (1986) such a configuration is unstable. Therefore we conclude that it is very likely that gravitational instability will set in as soon as the two stars have merged into one massive body within $t \gtrsim 3$–4 ms. General relativistic effects will certainly influence the transformation of the infall orbit of the neutron stars into a bound one; this needs to be studied with relativistic simulations.

2.) *Gravitational waves and neutrinos:* The gravitational-wave signal will certainly depend on general relativistic effects and our basically Newtonian models have only a limited ability to make predictions of a possibly measurable pulse. Moreover, the duration of the gravitational-wave and neutrino emission from the hot collision remnant will depend on the timescale of the delay until black hole formation. Our simulations yield a maximum amplitude of the gravitational waveform that is $h_{\max} \approx 2$–4×10^{-23} for neutron star collisions happening at a distance of 1 Gpc. The off-center collision is the stronger gravitational-wave source due to the larger quadrupole moment of the rotating system and the longer duration of the emission which might last for 10–20 wave periods in the 1000–2000 Hz range. The gravitational-wave strain would be close to the lower sensitivity limit of the new generation of gravitational-wave interferometers which are currently under construction and will start operation within the next years. Of course, neutron star collisions are very rare and very short events and therefore the chance to catch a signal is rather small. The head-on collision is the more powerful neutrino source of the two investigated cases and emits an energy about 3 times larger in neutrinos than in gravitational waves. The peak neutrino luminosity reaches $4 \times 10^{54}\,\mathrm{erg\,s^{-1}}$ and the total energy radiated in neutrinos within a few milliseconds is around 10^{52} erg.

3.) *Gamma-ray bursts:* Because of the larger energy output in neutrinos and the very high neutrino luminosity ($L_\nu \gtrsim 10^{54}\,\mathrm{erg\,s^{-1}}$) as well as high mean energies of the emitted neutrinos ($\langle\epsilon_\nu\rangle \lesssim 40$ MeV), the head-on collision provides more favorable conditions for producing gamma-ray bursts from e^+e^--photon fireballs created by $\nu\bar\nu$ annihilation. We calculate a conversion efficiency of neutrino energy into e^+e^--pairs of about 1% and find an integral value for the energy deposited in the vicinity of the collision remnant of 10^{50} erg within only 10 ms. However, most of this energy is deposited in the immediate neighbourhood of the neutrinospheres where the density is still higher than about $10^{10}\,\mathrm{g\,cm^{-3}}$. Therefore the baryon loading of the e^+e^--photon fireball is at least 5 orders of magnitude too high and instead of having values above 100 the relativistic Lorentz factor is estimated to be only around 10^{-3}. Dynamically ejected material together with a flow of baryonic matter driven by neutrino-energy transfer to the surface layers of the collision remnant are therefore a harmful poisonous combination which prevents relativistic expansion of the pair-plasma fireball even though the latter seems to obtain an interesting amount of energy from $\nu\bar\nu$-annihilation.

Strong shock heating of the neutron stars during their violent collision (or during their merging as suggested by post-Newtonian simulations, see Oohara & Nakamura 1997) can indeed raise the neutrino luminosities significantly and can thus enhance the energy deposition by $\nu\bar\nu$ annihilation. The associated dynamical ejection of gas and the neutrino-driven wind caused by the intense neutrino fluxes, however, impede the emergence of gamma-rays from this scenario. Fireballs powered by neutrinos from colliding neutron stars should therefore be ruled out as possible sources of cosmological gamma-ray bursts. Also, we do not see the formation of highly relativistic shocks during the collisions by which a fraction of 0.1–1% of the kinetic energy at impact ($\gtrsim 10^{53}$ erg) might be hydrodynamically focused into a small amount of mass ($\sim 10^{-6}$ to $10^{-5}\,M_\odot$). The expansion velocity of the collision shocks is at most a few tenths of the speed of light and the masses ejected in the presented models are more than 3 orders of magnitude too large to allow for ultrarelativistic motion.

Acknowledgements. M.R. is grateful to Sabine Schindler for her patience in their common office. We would like to thank M. Camenzind, W. Hillebrandt, F. Meyer, M. Rees, and S. Woosley for educative discussions. MR acknowledges support by the PPARC, HTJ by the "Sonderforschungsbereich 375-95 für Astro-Teilchenphysik" der Deutschen Forschungsgemeinschaft. The calculations were performed at the Rechenzentrum Garching on a Cray-YMP 4/64.

References

Berger M.J., 1987, SIAM J. Numer. Anal. 24, 967
Berger M.J., Colella P., 1989, JCP 82, 64
Berger M.J., Oliger J., 1984, JCP 53, 484
Bethe H.A., Brown G.E., 1998, preprint
Bildsten L., Cutler C., 1992, ApJ 400, 175
Blanchet L., Damour T., Schäfer G., 1990, MNRAS 242, 289
Centrella J.M., McMillan S.L.W., 1993, ApJ 416, 719
Colella P., Woodward P.R., 1984, JCP 54, 174
Dar A., Kozlovsky B.Z., Nussinov S., Ramaty R., 1992, ApJ 388, 164
Dokuchaev V.I., Eroshenko Yu.N., 1996, Astronomy Letters 22, 578
Dokuchaev V.I., Eroshenko Yu.N., Ozernoy L.M., 1998, astro-ph/9802358
Friedman J.L., Ipser J.R., Parker L., 1986, ApJ 304, 115
Friedman J.L., Ipser J.R., 1987, ApJ 314, 594
Goussard J.O., Haensel P., Zdunik J.L., 1997, A&A 321, 822
van den Heuvel E.P.J., Lorimer D.R., 1996, MNRAS 283, L37
Janka H.-Th., 1993, in: *Frontier Objects in Astrophysics and Particle Physics*, Conf. Proc. Vol. 40, eds. F. Giovannelli and G. Mannocchi, SIF, Bologna, p. 345
Katz J.I., Canel L.M., 1996, ApJ 471, 915
Kochanek C.S., 1992, ApJ 398, 234
Lai D., 1994, MNRAS 270, 611
Lattimer J.M., Swesty F.D., 1991, Nucl. Phys. A535, 331
Lipunov V.M., Postnov K.A., Prokhorov M.E., Panchenko I.E., Jørgensen H.E., 1995, ApJ 454, 593
Lipunov V.M., Postnov K.A., Prokhorov M.E., 1997, MNRAS 288, 245
Mao S., Narayan R., Piran T, 1994, ApJ 420, 171
Mészáros P., Rees M.J., 1992b, ApJ 397, 570
Narayan R., Piran T., Shemi A., 1991, ApJ 379, L17
Ogawaguchi W., Kojima Y., 1996, astro-ph/9610032
Oohara K., Nakamura T., 1997, astro-ph/9606179, in: *Relativistic Gravitation and Gravitational Radiation*, eds. J.-A. Marck and J.-P. Lasota, Cambridge Univ. Press, Cambridge, p. 309
Phinney E.S., 1991, ApJ 380, L17
Prokhorov M.E., Lipunov V.M., Postnov K.A., 1997, astro-ph/9704039
Rasio F.A., Shapiro S.L., 1992, ApJ 401, 226
Roy A.E., 1982, *Orbital Motion*, Adam Hilger Ltd, Bristol
Ruffert M., 1992, A&A 265, 82
Ruffert M., Janka H.-Th., Schäfer G., 1996, [RJS], A&A 311, 532
Ruffert M., Janka H.-Th., Takahashi K., Schäfer G., 1997, [RJTS], A&A 319, 122
Shaviv N.J., Dar A., 1995, MNRAS 277, 287
Tutukov A.V., Yungelson L.R., Iben I., 1992, ApJ 386, 197
Tutukov A.V., Yungelson L.R., 1993, MNRAS 260, 675
Wex N., 1995, Class. Quantum Grav. 12, 983
Wilson J.R., Mathews G.J., Maronetti P., 1996, Phys. Rev. D 54, 1317